

## Energy deposition and primary chemical products in Titan's upper atmosphere

P. Lavvas<sup>a,\*</sup>, M. Galand<sup>b</sup>, R.V. Yelle<sup>a</sup>, A.N. Heays<sup>c</sup>, B.R. Lewis<sup>c</sup>, G.R. Lewis<sup>d,e</sup>, A.J. Coates<sup>d,e</sup>

<sup>a</sup> Lunar and Planetary Laboratory, University of Arizona, Tucson 85721-0092, USA

<sup>b</sup> Department of Physics, Imperial College, London SW7 2AZ, UK

<sup>c</sup> Research School of Physical Sciences and Engineering, Australian National University, Canberra, ACT 0200, Australia

<sup>d</sup> Mullard Space Science Laboratory, University College London, Dorking RH5 6NT, UK

<sup>e</sup> Centre for Planetary Sciences, University College London WC1E 6BT, UK

### ARTICLE INFO

#### Article history:

Received 1 October 2010

Revised 24 January 2011

Accepted 2 March 2011

Available online 9 March 2011

#### Keywords:

Titan

Photochemistry

### ABSTRACT

Cassini results indicate that solar photons dominate energy deposition in Titan's upper atmosphere. These dissociate and ionize nitrogen and methane and drive the subsequent complex organic chemistry. The improved constraints on the atmospheric composition from Cassini measurements demand greater precision in the photochemical modeling. Therefore, in order to quantify the role of solar radiation in the primary chemical production, we have performed detailed calculations for the energy deposition of photons and photoelectrons in the atmosphere of Titan and we validate our results with the Cassini measurements for the electron fluxes and the EUV/FUV emissions. We use high-resolution cross sections for the neutral photodissociation of N<sub>2</sub>, which we present here, and show that they provide a different picture of energy deposition compared to results based on low-resolution cross sections. Furthermore, we introduce a simple model for the energy degradation of photoelectrons based on the local deposition approximation and show that our results are in agreement with detailed calculations including transport, in the altitude region below 1200 km, where the effects of transport are negligible. Our calculated, daytime, electron fluxes are in good agreement with the measured fluxes by the Cassini Plasma Spectrometer (CAPS), and the same holds for the measured FUV emissions by the Ultraviolet Imaging Spectrometer (UVIS). Finally, we present the vertical production profiles of radicals and ions originating from the interaction of photons and electrons with the main components of Titan's atmosphere, along with the column integrated production rates at different solar zenith angles. These can be used as basis for any further photochemical calculations.

© 2011 Elsevier Inc. All rights reserved.

### 1. Introduction

The photochemistry in Titan's atmosphere begins with the dissociation and ionization of the main atmospheric components, N<sub>2</sub> and CH<sub>4</sub>. Reaction among the fragments produced and the background gas provides the plethora of organic species detected in Titan's atmosphere, both neutrals (Coustonis et al., 2007) and ions (Vuitton et al., 2007) and eventually the optically dominating organic haze (Porco, 2005; Tomasko et al., 2008).

The dominant energy source available for accomplishing this dissociation in the upper atmosphere (above 500 km) is solar radiation, which is able to dissociate and ionize the neutral species. Moreover the energetic electrons produced during the photoionization have large enough energies to accomplish further dissociation and ionization. Magnetospheric electrons are another energy source for Titan's upper atmosphere. On the dayside, solar photons

have been shown to be the dominant source of ionization (Galand et al., 2006, 2010; Agren et al., 2009). On the nightside, the contribution by magnetospheric electrons has been found to be dominant at times (Cravens et al., 2009), but it is always much less than solar ionization on the dayside. The lack of EUV emissions from the nightside (Ajello et al., 2007, 2008) and the large day/night variation in the thermal electron density (Agren et al., 2009; Cui et al., 2009) suggest ionization and dissociation by magnetospheric electrons is weak or sporadic compared to solar EUV. Along with magnetospheric electrons, energetic ions (H<sup>+</sup>, O<sup>+</sup>) can also contribute to the dissociation of the neutral gases with their impact located between 500 and 1000 km depending on the ion mass. Yet, their contribution appears to be smaller than the impact of solar radiation and photoelectrons under typical Titan conditions; only flyby T5 had an enhanced magnetospheric signature that could provide an important ionization rate (Cravens et al., 2008). Between 700 and 500 km, the ablation of meteoroids provides a contribution to the ionization (Kliore et al., 2008), but this is small compared to all other sources when integrated along an atmospheric column, and furthermore mainly associated with

\* Corresponding author.

E-mail address: [lavvas@lpl.arizona.edu](mailto:lavvas@lpl.arizona.edu) (P. Lavvas).

ionization of the meteoroid material (Molina-Cuberos et al., 2001). Finally, in the lower atmosphere, galactic cosmic rays (GCR) are able to ionize the neutral gas species with a peak contribution close to 65 km (Lopez-Moreno et al., 2008) and a magnitude comparable to ionization by solar photons in the upper atmosphere. For a more detailed discussion of energy sources in Titan's atmosphere see also Sittler et al. (2009, 2010) and references therein.

High quality Cassini observations of the distribution of photochemical constituents have raised the bar for Titan photochemical models. In particular most of the early models treated the initial photodissociation and ionization of the atmosphere in an approximate or limited way. The discovery of a complex ionosphere (Vuitton et al., 2007, 2008) as well as abundant N-bearing species (Yelle et al., 2010) and isotopic anomalies (Liang et al., 2007), implies that careful treatment of dissociation and ionization of the major constituents is required for accurate photochemical models. Furthermore, Cassini instruments provide observations for the thermal and suprathermal electron populations in the atmosphere and their energy distribution, which can now be used for the quantitative validation of the models and the investigation of the photoelectron contribution in the atmospheric chemical processes. To this end, we present here a detailed model for photodissociation and ionization of  $N_2$  and  $CH_4$  incorporating the latest photoabsorption cross sections and including the contribution of photoelectrons to the dissociation and ionization.

UV emission rates also constrain energy deposition rates. During photoabsorption or in collision with suprathermal electrons, nitrogen can be excited or dissociated providing atomic N in an excited state. Spontaneous irradiation produces emissions in the EUV and FUV spectral regions (airglow) that can be used to discriminate the separate roles of photons and photoelectrons. The analysis of the Voyager I EUV emissions demonstrated the importance of photoelectrons in the reproduction of the emissions by optically forbidden transitions (e.g. the Lyman–Birge–Hopfield, (LBH), band). Also they set constraints on the role of magnetospheric electrons by comparison of the relative day/night emissions (Strobel and Shemansky, 1982; Strobel et al., 1991). Due to the low resolution of the Voyager measurements and our insufficient knowledge, at that time, of the transitions involved in the predissociation of  $N_2$ , the role of photoelectrons was overestimated. Improvement on the relative contribution of photons and photoelectrons was achieved through theoretical calculations (Stevens, 2001). The calculations are verified by the higher resolution emission spectra measured by the Cassini UltraViolet Imaging Spectrometer (UVIS). These high-resolution emissions can also be used for the validation of the photoelectron degradation calculations.

In this work we focus on the upper atmosphere and investigate the role of photons and photoelectrons in the dissociation of the main gas composition in Titan's atmosphere. We present below detailed theoretical calculations for the photodissociation and photoionization of  $N_2$  and  $CH_4$  based on the most recent and accurate photon absorption cross sections from both laboratory and theoretical investigations. The calculations include photoelectron energy degradation using a local energy deposition model. This model was briefly described in Vuitton et al. (2009), but here we provide a complete description of its derivation (Section 2). In addition, we have updated our electron impact cross sections with the most recently published results, and we report on the contribution of photoelectrons in the dissociation of  $N_2$  and  $CH_4$ . We validate our models against the recent Cassini measurements for the suprathermal electron fluxes and the observed EUV and FUV emission spectrum (Section 3). Our results show that the contributions of both photons and photoelectrons are required for the accurate representation of the chemical precursors in Titan's upper atmosphere (Section 4).

## 2. Photolysis

Methane and nitrogen are dissociated by photons with wavelengths  $\lambda < 1350 \text{ \AA}$  and  $\lambda < 1000 \text{ \AA}$ , respectively. In our calculations, we determine the atmospheric optical depth by integration along the line of sight, assuming a spherical atmosphere. Here, we describe the  $N_2$  cross sections focusing on the new theoretical cross sections for neutral dissociation, similar to those employed recently by Liang et al. (2007) for the study of N-isotope anomalies in HCN on Titan.

The dipole-allowed photoabsorption spectrum of molecular nitrogen, which starts near  $1000 \text{ \AA}$ , is due to transitions from the ground state  $X^1\Sigma_g^+$  into strongly-coupled electronically-excited valence and Rydberg states of  $^1\Pi_u$  and  $^1\Sigma_u^+$  symmetry. The resultant spectrum consists predominantly of multiple narrow band systems, but coupling between the discrete and continuum states, with only minor exceptions, results in widespread predissociation which yields photofragments invariably with a high degree of internal excitation. Here, we use  $N_2$  photoabsorption cross sections computed using a coupled-channel Schrödinger equation (CSE) quantum-mechanical model, which treats the interactions between the excited states explicitly. Aspects of the model, which has been applied to the study of planetary-atmospheric problems (Liang et al., 2007; Liu et al., 2009) have been described in detail elsewhere (Lewis et al., 2005, 2008a,b; Haverd et al., 2005). The CSE model is validated experimentally and the resultant cross sections are inherently of infinite resolving power. Furthermore, the computation of self-consistent temperature-dependent and isotopic cross sections is simple and reliable. Due to the highly structured nature of the  $N_2$  photoabsorption and the solar spectrum, both of which are illustrated in Fig. 1, the correct calculation of atmospheric penetration and  $N_2$  photolysis rates clearly require very high spectral resolution.

The lowest three dissociation limits for  $N_2$ , i.e.,  $N(^4S) + N(^4S)$  at  $1270 \text{ \AA}$ ,  $N(^2D) + N(^4S)$  at  $1021 \text{ \AA}$ , and  $N(^2P) + N(^4S)$  at  $930 \text{ \AA}$ , are not accessible via allowed predissociation mechanisms. Predissociation has never been observed to the lowest limit,  $N(^4S) + N(^4S)$  (Walter et al., 1993), while the mechanisms accessing the other two limits must necessarily involve spin-orbit coupling to triplet states, as demonstrated by Lewis et al. (2005) for predissociation of the lowest-energy  $^1\Pi_u$  states. The present CSE model includes spin-orbit and rotational couplings which provide a realistic treatment of the  $N_2$  predissociation, including strong vibrational and rotational variations, especially at the longer wavelengths. Qualitatively consistent with the detailed observations of Walter et al. (1993), the computed dissociation branching ratios between the  $N(^2P) + N(^4S)$  and  $N(^2D) + N(^2D)$  limits display a complex behavior, predominantly favoring the lower limit for  $1021 \text{ \AA} > \lambda > 891 \text{ \AA}$ , and the higher for  $891 \text{ \AA} > \lambda > 854 \text{ \AA}$ . The first allowed predissociation channel for  $N_2$ , i.e., involving singlet-singlet coupling, opens at the  $N(^2D) + N(^2D)$  dissociation limit and branching to this limit can be safely assumed to dominate for  $\lambda < 854 \text{ \AA}$ . Because of remaining uncertainties in the branching mechanisms at shorter wavelengths, we have adopted the following simplified assumptions for the dissociation products:

$$\begin{aligned} 1021 \text{ \AA} > \lambda > 891 \text{ \AA} &: N(^2D) + N(^4S) \\ 891 \text{ \AA} > \lambda > 854 \text{ \AA} &: N(^2P) + N(^4S) \\ \lambda < 854 \text{ \AA} &: N(^2D) + N(^2D) \end{aligned}$$

Moreover, the lifetime of  $N(^2P)$  is very small and rapidly de-excites to the longer lived  $N(^2D)$  state (Zipf et al., 1980). In addition  $N(^2P)$  is chemically less active than  $N(^2D)$  (Herron, 1999) and affects the following chemistry to a smaller degree. Based on these arguments, and also because the production of  $N(^2P)$  relative to  $N(^2D)$  is not well constrained by measurements, both for photons and

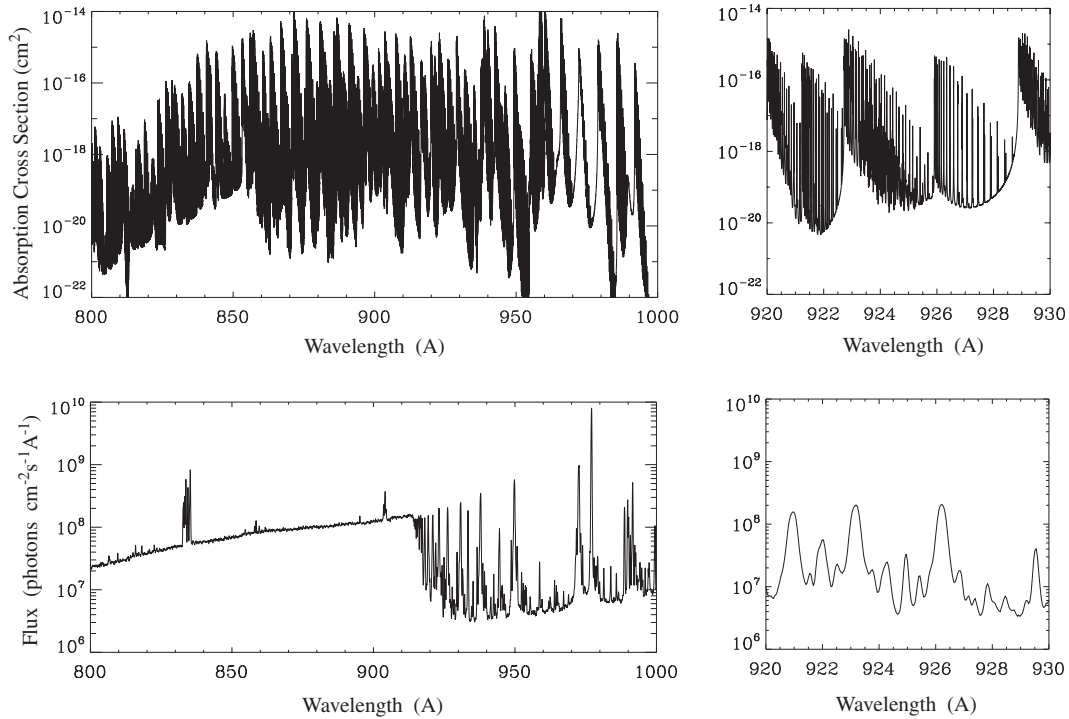


**Fig. 1.** The theoretically calculated cross sections presented here for  $N_2$  photoabsorption between 800 and 1000 Å (upper left panel) with a resolution of  $0.05 \text{ cm}^{-1}$  (corresponding to  $3\text{--}5 \times 10^{-5} \text{ Å}$ ) and the high resolution ( $0.04 \text{ Å}$ ) solar flux spectrum from the SOHO/SUMER instrument at 1 AU (lower left panel). The two small panels on the right show the structure of the cross sections and solar flux in the narrow region between 920 and 930 Å.

photoelectrons, we assume in the calculations that all  $N(^2P)$  formed results to  $N(^2D)$ .

The CSE cross sections are quantitative over the longer wavelength region of the spectrum, but their accuracy is expected to decrease at shorter wavelengths due to the omission of higher-principal-quantum-number Rydberg states in the current model (Liang et al., 2007). This is confirmed by comparison with laboratory measurements. In Fig. 2, we compare the experimental

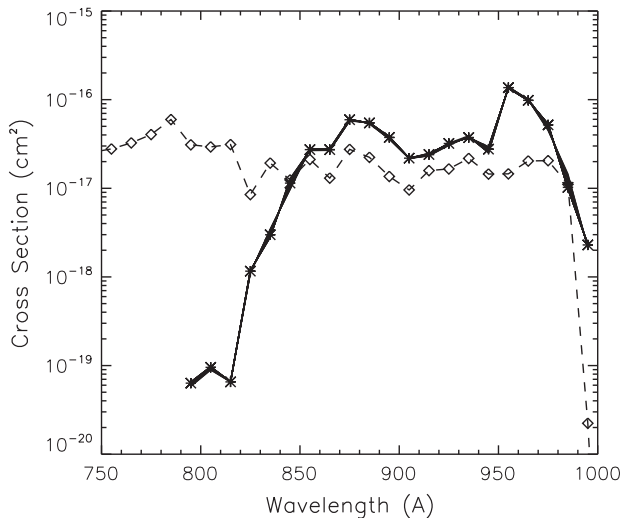


**Fig. 2.** The high resolution photoabsorption cross sections of  $N_2$  from the present work, convolved to the low resolution ( $10 \text{ Å}$ ) model spectrum (asterisks). The thickness of the solid line presents the temperature variation of the cross section between 50 and 500 K. The  $N_2$  photoabsorption cross sections from Samson et al. (1989), convolved to the same resolution is presented by the diamonds.

room-temperature cross section of Carter (1972), as tabulated in Fennelly and Torr (1992), with the relevant CSE cross section. Both sets have been convolved to a resolution of  $10 \text{ Å}$  full-width at half-maximum (FWHM) for the comparison. The two sets appear to be in relative agreement for  $\lambda > 845 \text{ Å}$ , but for shorter wavelengths the CSE cross section decreases sharply relative to the experimental cross section. For this reason, we have used the computed CSE cross sections for  $\lambda > 845 \text{ Å}$ , but experimental cross sections at shorter wavelengths. The impact of the atmospheric temperature on the computed CSE cross sections is also taken into account.

Before proceeding, it is important to note that the existing experimental cross sections in the highly-structured regions of the spectrum are compromised significantly by the effects of limited instrumental resolving power. In particular, the measurements of Carter (1972) were taken at a resolution of  $0.04 \text{ Å}$  FWHM and the resulting cross sections are pressure dependent, representing a lower limit to the true cross sections. The systematic difference between the computed and experimental cross sections in the longer wavelength region of Fig. 2 is thus explained. It follows that the biggest deficiency in our adopted cross sections is the use of currently available experimental results in the structured spectral regions with  $\lambda < 845 \text{ Å}$ . It will be possible to extend the CSE calculations to shorter wavelengths by the inclusion of further Rydberg states, but this approach will only cover part of the gap between  $845 \text{ Å}$  and the ionization limit at  $796.8 \text{ Å}$ . Therefore, supplementary high-resolution absolute experimental cross sections will still be necessary to overcome the identified deficiency. Such data is likely to become available through the use of a unique EUV Fourier-transform spectrometer, recently installed at the SOL-EIL synchrotron in France, with a resolution of  $\sim 0.001 \text{ Å}$  FWHM, sufficient to define even the narrowest Doppler-limited lines in the  $N_2$  spectrum.

The threshold for  $N_2^+$  formation is at  $796.8 \text{ Å}$  ( $15.58 \text{ eV}$ ), and at this energy  $N_2^+$  is produced in its ground state ( $X^2\Sigma_g^+$ ). Higher

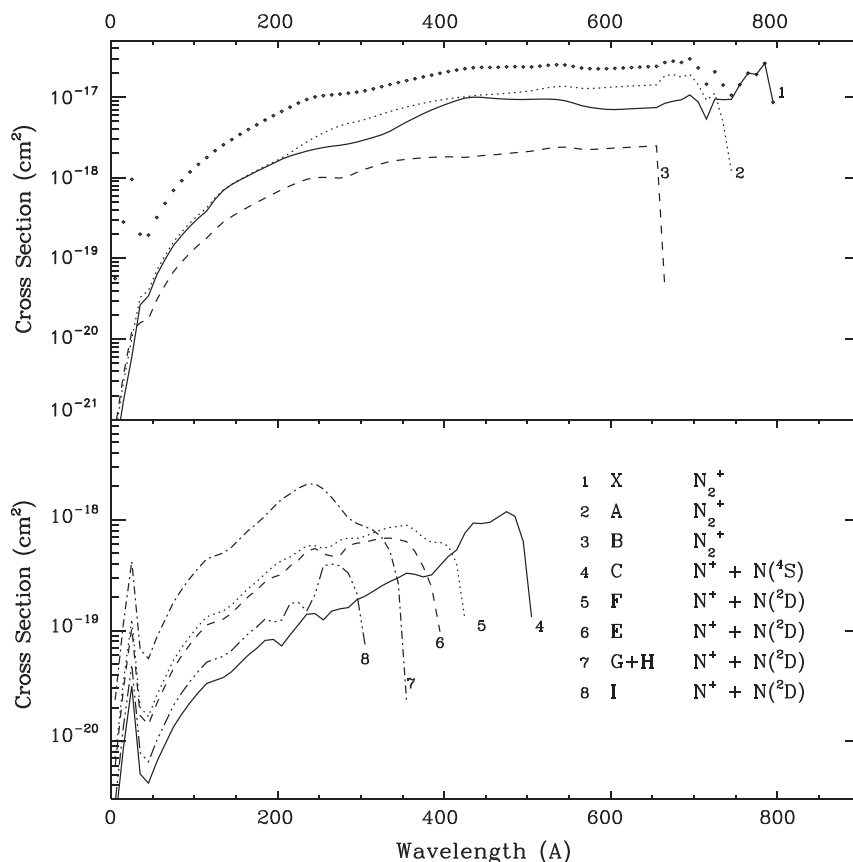


**Fig. 3.**  $N_2$  cross sections for ionization and dissociative ionization. The diamonds correspond to the total ionization cross section, while the rest of the lines present partial ionization cross sections to different states.

photon energies lead to the production of the  $N_2$  ion at excited states (Fig. 3). The analysis of the emerging photoelectron spectra shows specific band formation that is correlated with the excitation of the ions to specific states depending on the energy of the photons (see Table 1). For wavelengths smaller than 510 Å (24.3 eV) the excited  $N_2^+$  ions have enough energy to dissociate initiating the dissociative photoionization. The ionization of the valence electrons leading to the X, A and B bands leads to the formation of  $N_2^+$ , while the ionization of the inner-valence electron leads to production of the C, F, E, G and H bands which are related to the dissociative photoionization. The total ionization and dissociative ionization cross sections have been measured by Samson et al. (1987), while the cross sections for the excitation of the  $N_2^+$  ions at the different bands originating from the inner-valence electrons have been reported by Krummacher et al. (1980) for the C, F, E and the combined G + H bands. In the calculations we have

**Table 1**  
Band nomenclature of the  $N_2$  ionization emerging photoelectrons and the threshold energy. Data from Baltzer et al. (1992) and Krummacher et al. (1980).

| Band            | Threshold energy (eV) | Products            |
|-----------------|-----------------------|---------------------|
| $X^2\Sigma_g^+$ | 15.58                 | $N_2^+$             |
| $A^2\Pi_u$      | 16.926                | $N_2^+$             |
| $B^2\Sigma_u^+$ | 18.751                | $N_2^+$             |
| $C^2\Sigma_u^+$ | 25.514                | See text            |
| $F^2\Sigma_g^+$ | 28.8                  | $N^+(^3P) + N(^2D)$ |
| $E^2\Sigma_g^+$ | 33.6                  | $N^+(^3P) + N(^2D)$ |
| G + H           | 36.8                  | $N^+(^3P) + N(^2D)$ |

normalized the cross sections of Krummacher et al. (1980) to the total dissociative ionization cross sections reported by Samson et al. (1987). The state of the dissociation fragments produced depends also on the photon energy. This has been investigated by Nicolas et al. (2003) for the C band and by Aoto et al. (2006) for higher bands. For the C band, from the dissociation limit up to 473 Å (26.19 eV) the products are  $N^+(^3P) + N(^4S)$ , while at smaller wavelengths until 464.6 Å (26.68 eV) the yield for the last channel drops to 40% and the rest 60% is in the  $N^+(^1D) + N(^4S)$  channel. The authors also report a narrow region between 26.275 and 26.3 eV where the two channels have equal yields. At even lower energies the dissociation products are in the  $N^+(^3P) + N(^2D)$  states. For the other bands the measurements of Aoto et al. (2006) suggest that the emerging dissociation products can be at different states as the ionization energy increases. In the calculations we consider production only in the  $N^+(^3P) + N(^2D)$  states.

The cross sections for the photolysis of methane are taken from different laboratory investigations depending on the wavelength region investigated (Fig. 4). Photoionization and dissociative photoionization cross sections were measured by Samson et al. (1989) between 110 and 950 Å and provide yields for all the main dissociation products. The main ion fragments produced at all wavelengths are  $CH_4^+$  and  $CH_3^+$ .  $CH_2^+$  production starts at 816.0 Å (15.2 eV) accompanied with a hydrogen molecule. Below 630.3 Å (19.67 eV) the hydrogen molecule can be further dissociated to atomic hydrogens, but whether this happens or not cannot be retrieved from the observations. In the calculations we assumed that below 630.3 Å we have 50% yield for each of the two processes. For all the other dissociation ion products we assume

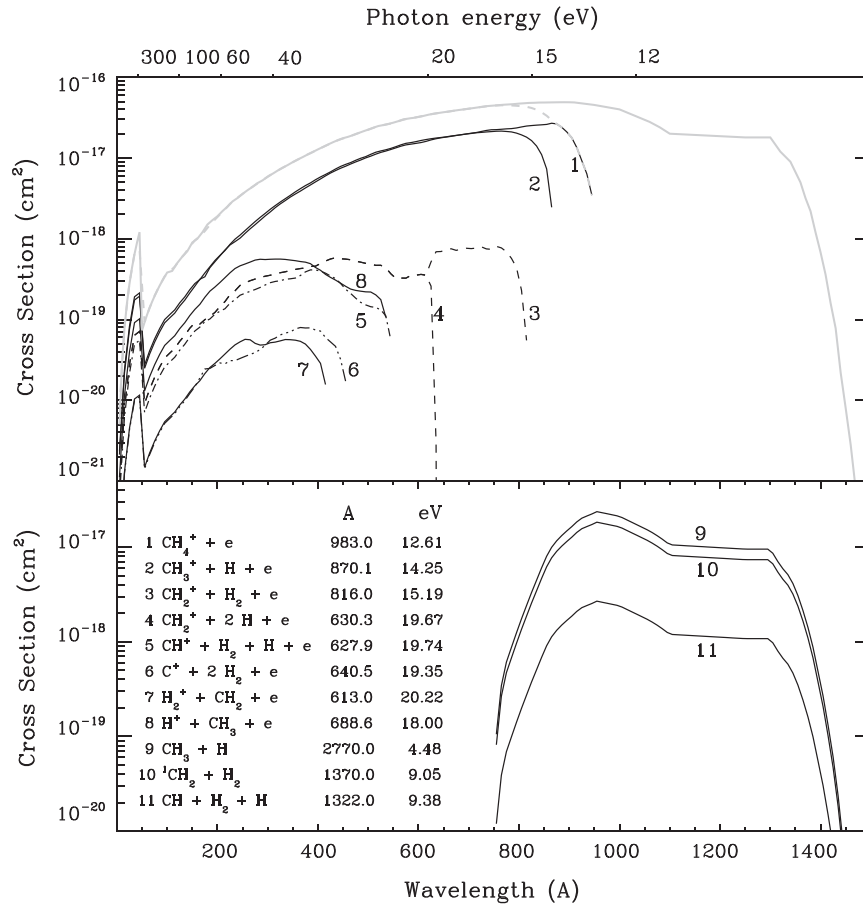


**Fig. 4.** CH<sub>4</sub> photolysis cross sections. The gray lines correspond to the total absorption (solid gray) and total ionization cross sections (dashed gray), while the numbers present different ionization products summarized in the caption along with the adiabatic thresholds of each channel. For channels 3 and 4 the cross sections are the same for energies larger than 20 eV.

the neutral products to be those at the first threshold energy, although further dissociation can produce different neutral fragments at higher energies (see Table 5 in Samson et al., 1989). The absorption cross section for wavelengths below the C K-edge (43.68 Å) can be described by the functional:

$$\ln \sigma \text{ (Mb)} = 2.494 \times \ln[\lambda(\text{Å})] - 9.307 \quad (1)$$

while the cross sections at lower energies are taken from other laboratory measurements described in Samson et al. (1989). The yields for the different channels below 110 Å are assumed to remain constant to the measured values at 110 Å. At lower energies, neutral photodissociation is assumed to provide fragments based on the laboratory measurements of Wang et al. (2000) at Ly- $\alpha$  (Table 2). The total photoabsorption cross sections above the ionization threshold are taken from Lee and Chiang (1983) and Mount et al. (1977).

**Table 2**  
Methane photolysis products at Ly- $\alpha$ .

| Products                                      | Yield |
|---|-------|
| CH <sub>3</sub> + H                           | 0.291 |
| <sup>1</sup> CH <sub>2</sub> + H <sub>2</sub> | 0.584 |
| <sup>1</sup> CH <sub>2</sub> + 2H             | 0.055 |
| CH + H <sub>2</sub> + H                       | 0.070 |

### 3. Suprathermal electrons

The photoionization of a neutral species leads to the production of a positive ion along with a free electron (photoelectron). Depending on the energy of the ionizing radiation, the released photoelectron can have energies varying from almost zero kinetic energy for photons corresponding to energies very close to the ionization threshold up to a few keV for X-ray photons. The suprathermal electrons collide with neutral species, producing secondary ionization events (new electrons released are called secondary electrons) and the cascade continues until the electrons have energies smaller than the ionization thresholds of the neutral species. In order to calculate the contribution of suprathermal electron impact in the ionization of the neutral atmosphere we first need to know the production rate of photoelectrons at a specific energy ( $E$ ) and altitude ( $z$ ) from the solar radiation,  $S_{\odot}(z, E)$ . This can be calculated from:

$$S_{\odot}(z, E) = \sum_{kj} \Phi_{\odot}(z, \lambda) \sigma_{kj}^{hy}(\lambda) n_k(z) / \Delta E_{\lambda} \quad (2)$$

with  $\Phi_{\odot}(z, \lambda)$  the solar flux at altitude  $z$  and wavelength  $\lambda$ ,  $\sigma_{kj}^{hy}(\lambda)$  the photoabsorption cross section of species  $k$  for photoionization process  $j$  associated with an ionization potential  $T_j$ ,  $n_k(z)$  the neutral density of species  $k$ , and  $\Delta E_{\lambda}$  is the corresponding energy width in eV of the wavelength spectrum. The energy of the produced photoelectron is  $E = E_{\lambda} - T_j$ . The sum extends over all ionization processes  $j$  and neutral species  $k$ .

The degradation of photoelectrons is described by the Boltzmann equation (e.g. Rees, 1989):

$$\begin{aligned} \mu \frac{\partial I(z, \mu, E)}{\partial z} = & S_{\odot}(z, \mu, E) + n_e(z) \frac{\partial [L(E)I(z, \mu, E)]}{\partial E} \\ & + 2\pi \sum_{kj} \int_E^{\infty} \int_{-1}^1 d\mu' dE' R_{kj}(\mu', E'; \mu, E) I(z, \mu', E') \\ & - 2\pi \sum_{kj} \int_0^E \int_{-1}^1 d\mu' dE' R_{kj}(\mu, E; \mu', E') I(z, \mu, E) \end{aligned} \quad (3)$$

where  $\mu$  is the cosine of the pitch angle and  $I$  is the electron intensity ( $\text{cm}^{-2} \text{s}^{-1} \text{sr}^{-1} \text{eV}^{-1}$ ). The first term on the right hand side of the equation is the photoelectron source function ( $\text{cm}^{-3} \text{s}^{-1} \text{sr}^{-1} \text{eV}^{-1}$ ), the second term describes the energy transfer from suprathermal electrons to thermal electrons through Coulomb collisions using a stopping function  $L(E)$  discussed below, and the last term is the loss of energy  $E$  electrons due to all inelastic collisions. The third term on the right hand side describes the degradation of electrons of energy higher than  $E$  through collisions with neutral species  $k$  that can lead to production of neutrals in excited states, ionization and dissociation of neutrals and the production of secondary electrons (the  $j$  index discriminates among all these options).  $R_{kj}(\mu', E'; \mu, E)$  is the redistribution function of species  $k$  for process  $j$  and is further explained below. Solving this equation for the energy, angle and altitude distribution of electrons is not an easy task and requires multi-stream discrete ordinate methods (see e.g. Galand et al., 1999 and references therein).

In order to avoid this complexity we can assume that all locally produced photoelectrons degrade in the same region (no transport effects). Under this assumption (local approximation) the left hand side of the Eq. (2) is zero. Integration over solid angles then gives:

$$\begin{aligned} 0 = & \bar{S}_{\odot}(z, E) + n_e(z) \frac{\partial [L(E)\Phi(z, E)]}{\partial E} \\ & + (2\pi)^2 \sum_{kj} \left\{ \int_E^{\infty} \int_{-1}^1 d\mu d\mu' dE' R_{kj}(\mu', E'; \mu, E) I(z, \mu', E') \right. \\ & \left. - \int_0^E \int_{-1}^1 d\mu d\mu' dE' R_{kj}(\mu, E; \mu', E') I(z, \mu, E) \right\} \end{aligned} \quad (4)$$

where  $\Phi$  is the omnidirectional flux of electrons  $\Phi = 2\pi \int_{-1}^1 I d\mu$  ( $\text{cm}^{-2} \text{s}^{-1} \text{eV}^{-1}$ ). If the redistribution function ( $R$ ) is isotropic the above reduces to an energy dependent only equation:

$$\begin{aligned} 0 = & \bar{S}_{\odot}(z, E) + n_e(z) \frac{\partial [L(E)\Phi(z, E)]}{\partial E} + \sum_{kj} \int_E^{\infty} dE' R_{kj}(E'; E) \Phi(z, E) \\ & - \sum_{kj} \int_0^E dE' R_{kj}(E; E') \Phi(z, E) \end{aligned} \quad (5)$$

The last term of Eq. (5) can be replaced by the total electron collision cross section at energy  $E$ ,  $\sigma_k^T(E)$  for each species  $k$ , giving eventually:

$$\begin{aligned} 0 = & \bar{S}_{\odot}(z, E) + n_e(z) \frac{\partial [L(E)\Phi(z, E)]}{\partial E} \\ & + \sum_{kj} \int_E^{\infty} dE' R_{kj}(E'; E) \Phi(z, E') - \sum_k \sigma_k^T(E) n_k(z) \Phi(z, E) \end{aligned} \quad (6)$$

In the above,  $\bar{S}_{\odot}$  is the production of photoelectrons integrated in all directions. Assuming that the photoionization of neutral species produces photoelectrons symmetrically:

$$S_{\odot}(z, \mu, E) = \frac{1}{4\pi} S_{\odot}(z, E) \quad (7)$$

then  $\bar{S}_{\odot} = S_{\odot}(z, E)$ . Below we discuss the remaining parameters required for the photoelectron degradation calculations and compare

our local approximation model results with detailed solutions of the Boltzmann equation that includes the electron transport effects. This allows us to validate the local approximation as well as to identify its limitations.

### 3.1. Collisions with thermal electrons

Electrons with energies larger than 10 eV are degraded mainly through inelastic collisions with the neutral species. For smaller energies the excitation of neutral species has small cross sections and energetic electrons are degraded through collisions with the ambient thermal electrons (Coulomb interactions). The collisions between suprathermal and thermal electrons are described by the stopping function,  $L(E)$  (Stamnes and Rees, 1983). The stopping function is mainly controlled by the characteristic temperature of the thermal electron population.

### 3.2. Inelastic collisions with neutral species

The redistribution function  $R(E', E)$  describes the probability an electron of energy  $E'$ , colliding with a neutral species, to emerge with energy  $E$ . The possible processes affecting the energy redistribution of the electrons are excitation, dissociation and ionization with the latter coupled with the production of a secondary electron. For each process the redistribution function takes a different form (Table 3). In excitations, a collision (with a cross section  $\sigma_{ext}$ ) leaves the neutral species in an excited state and the electron loses only the energy required to excite the molecule to a given state with energy  $W$ . Thus, the redistribution function is a delta function satisfying the energy balance before and after the collision:

$$E' = E + W \quad (8)$$

If the neutral species is ionized by the incident electron then the remaining energy of the primary electron after the collision depends on the energy of the emerging secondary electron ( $E_s$ ), while the total energy is again conserved:

$$E' = E + E_s + T \quad (9)$$

with  $T$  the ionization potential of the neutral species for a given state. The energy distribution of the emerging secondary electrons is described by the differential cross section,  $\sigma(E_s, E')$  that must satisfy the relationship:

$$\sigma_{ion}(E') = \int_0^{E'} \sigma(E_s, E') dE_s \quad (10)$$

where  $\sigma_{ion}$  is the ionization cross section at the energy of the incident electron. For secondary electron production the differential cross section has been analytically described by fitting experimental results (see Rees, 1989). Inclusion in the calculation of these parameters and of the electron impact cross sections discussed in Appendix A, allows the simulation of the electron degradation.

**Table 3**  
Redistribution functions for different processes.

| Electron impact process  | $R(E, E')$                                 |
|--------------------------|--|
| Excitation of neutrals   | $\delta(E' - (E + W))\sigma_{ext}(E')n(z)$ |
| Dissociation of neutrals | Same                                       |
| Ionization of neutrals   | $\sigma_{ion}(E, E')n(z)$                  |
| Secondary electrons      | $\sigma_{sec}(E, E')n(z)$                  |

### 3.3. Local deposition – transfer equation comparison

In order to compare our local approximation model with solution of the complete Boltzmann equation we used the same input parameters for the two simulations. The common neutral density profiles and thermal electron populations correspond to the Titan T40 flyby discussed in detail below. We used the same photoelectron source distribution in the calculations avoiding the possible differences in the photon flux attenuation processes (the solar zenith angle was set to 37.5°). The resulting energetic electron flux distribution as a function of energy at different altitudes and the production rates for primary and secondary electrons are presented in Fig. 5.

The results show that there is very good agreement between the two simulations for both the electron fluxes and production rates, for altitudes below 1200 km. The electron flux energy distribution is characteristic of the input photoelectron production. For energies larger than 50 eV the electron flux is dominated by the production from X-ray deposition. These photons are able to penetrate deep in the atmosphere of Titan reaching altitudes below 800 km and this is why their signature in the electron energy distribution can be seen on all spectra. The peak deposition of X-rays is between 700 and 800 km, explaining the shoulder in the secondary electron production profile in this region. In mid energy range between 10 and 50 eV the energy distribution is dominated by the peak close to 24 eV. This is produced by the strong Hell solar line (304 Å) which is able to ionize N<sub>2</sub> providing N<sub>2</sub><sup>+</sup>; it is further discussed below in the comparison with the Cassini data. The Hell line is mainly absorbed close to 1000 km, thus, explaining the reduction of this feature at lower altitudes. Finally at lower energies the energy distribution of the electrons is dominated by the N<sub>2</sub> vibrational excitation between 2 and 3 eV present on all spectra.

The local approximation used in the current calculations has its limitations. For high neutral densities the collisions between energetic electrons and gas species are rapid enough to spatially constrain their energy deposition in the local region of photoelectron production. As the atmospheric density decreases with altitude, the collisions between the energetic electrons and the neutral species become less frequent and the former can diffuse in the atmosphere for large distances among collisions. This effect is evident in the comparison between the electron fluxes calculated with the two methods at altitudes above 1200 km. The same is also clear in the altitude profile of the secondary electron production rate (Fig. 5b) with the rate calculated by the local approximation being larger than the transport solution rate above 1200 km. Such an

effect was also observed in electron transport calculations for the Earth’s atmosphere (Cicerone et al., 1973). It is interesting to note in the electron fluxes comparison that a small deviation between the two solutions is seen for small energies at low altitudes as well. This happens because the electron impact cross sections at these energies are small relative to higher energies and thus a small contribution by transport can emerge. This effect does not reflect in the production rates due to the low energy of these electrons.

The transition region between the local energy deposition and the transport-affected domain is also affected by the solar zenith angle. For large  $\mu$  photons can penetrate to deeper altitudes, thus, the photoelectron production is shifted to regions of high density where the local approximation holds. As the solar zenith angle increases the photoelectron production moves towards higher altitudes and the relative contribution of transport effects can increase.

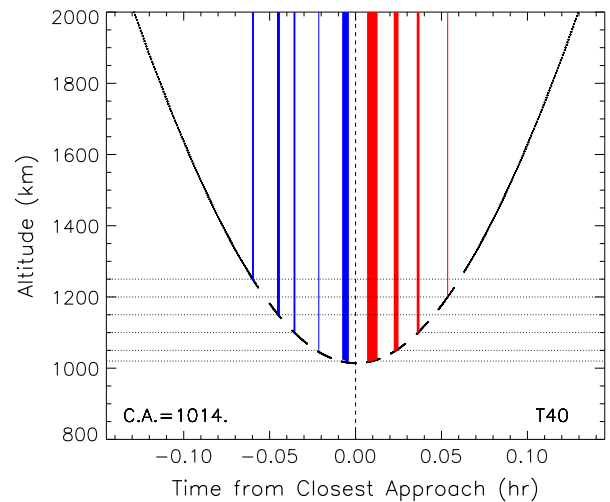


**Fig. 6.** Cassini spacecraft trajectory during T40 flyby (black thick dots). The time corresponds to the spacecraft time in hours. The local time at closest approach was 14.3 h. The gaps correspond to the time intervals where the actuator was in the ram direction and negative ions were detected. The blue and red shaded regions present the time intervals for which CAPS measurements are compared with the model results for the ingress (blue) and egress (red) parts of the flyby. The dotted lines correspond to the average altitude for each set of measurements used. (For interpretation of the references to color in this figure legend, the reader is referred to the web version of this article.)

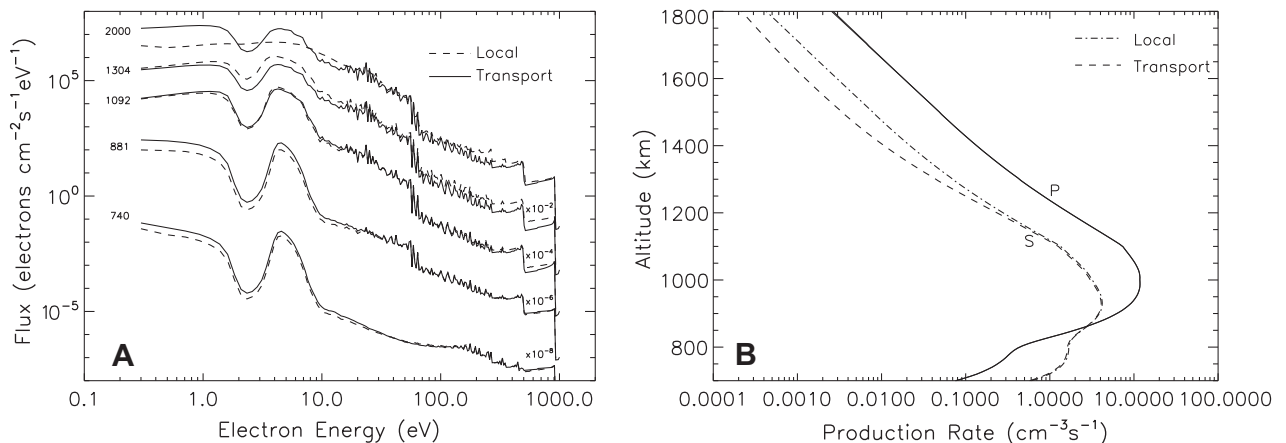


**Fig. 5.** Panel A: Comparison between local approximation model and transport calculations at different altitudes. Note that the distributions for different altitudes have been shifted downwards for clarity by the designated factors. Panel B: Primary and secondary electron production rates for the local approximation and transport calculations.

#### 4. Observational constraints

The Cassini spacecraft provided *in situ* measurements for the suprathermal electron fluxes and EUV/FUV emissions in Titan's atmosphere which can be used for validation of our simulations. These are presented below.

##### 4.1. Cassini CAPS/ELS

The CAPS/ELS instrument measures the electron fluxes along the spacecraft trajectory during each Titan flyby (Coates et al., 2007, 2010; Lewis et al., 2010). We validate our electron fluxes model against the T40 flyby measurements, which took place on January 5, 2008, on Titan's dayside with a solar zenith angle of  $37.5^\circ$  at closest approach (1014 km). We use the neutral densities of  $N_2$  and  $CH_4$  measured by INMS for this flyby and scale them upward by a constant factor of 2.6 which is found necessary in order to have the INMS measured densities in agreement with the atmospheric density derived by the HASI and the Cassini Attitude and Articulation Control Subsystem (AACCS) observations (Müller-Wo-

darg et al., 2008; Strobel et al., 2009). During this flyby CAPS also detected the presence of negative ions, when the actuator of the instrument was pointing in the ram direction of the spacecraft (Fig. 6). Thus, we can compare the simulations with the measurements only at altitudes not affected by the negative ions. The largest number of spectra available for the averaging is found around the closest approach.

The comparison between the model and observations can be separated into three energy regions (Fig. 7):  $E < 5$  eV,  $5 \text{ eV} < E < 15$  eV, and  $E > 15$  eV. The best agreement between the model and the observations takes place in the second energy region ( $5 \text{ eV} < E < 15$  eV) where both the magnitude and energy dependence of the differential electron flux are well reproduced. The local peak close to 24 eV is due to the HeII (304 Å) solar line which provides a strong photoelectron production at this energy range. This feature is composed of three peaks (see Fig. 8) originating from the ionization of  $N_2$  in the three valence states (X, A, and B), but these cannot be resolved by the energy resolution of the CAPS instrument ( $\Delta E/E = 16.7\%$ ).

For larger energies the model predicts a sharp decrease in the electron flux, although the observations suggest a significantly lar-

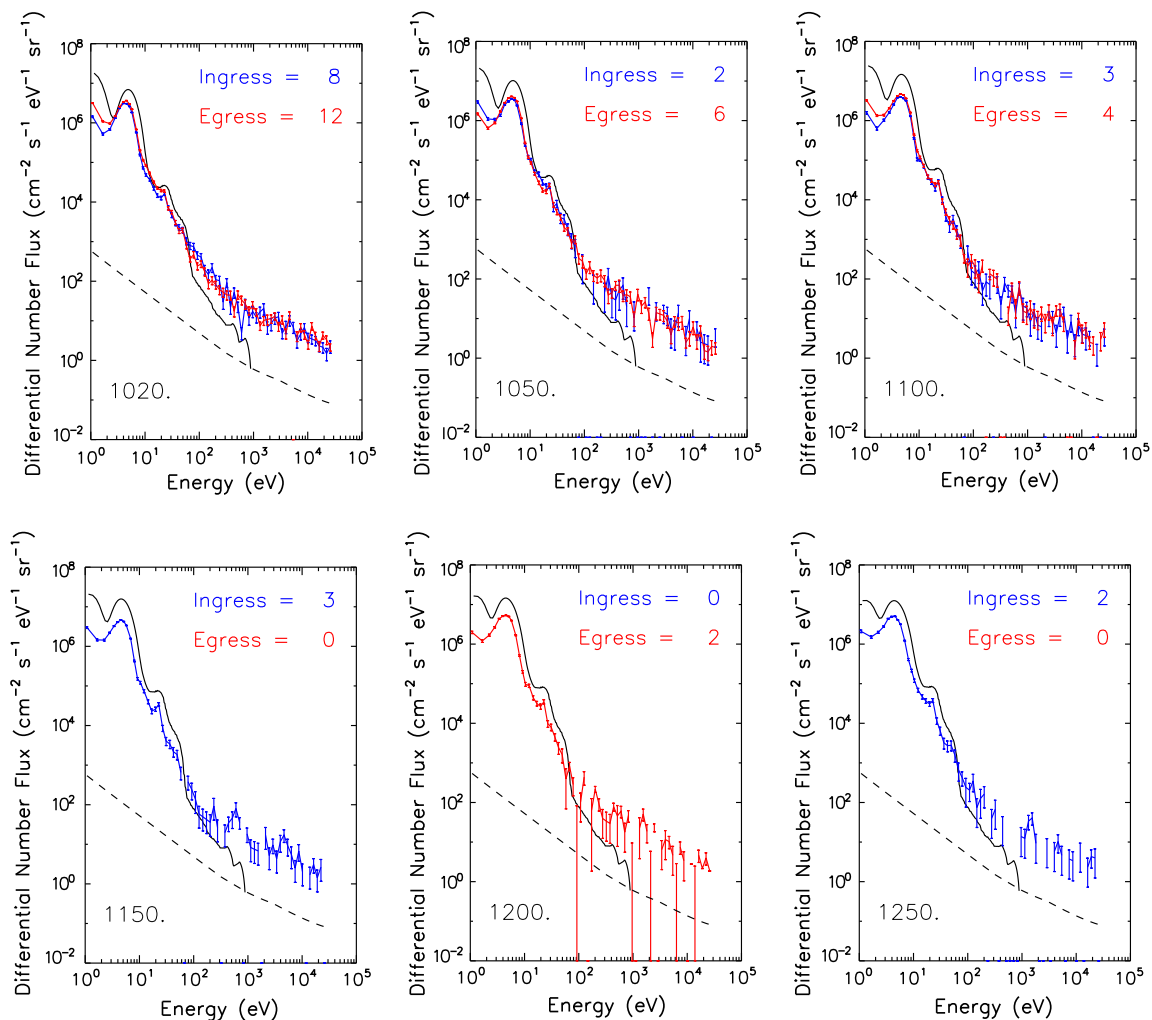


**Fig. 7.** Comparison between measured and calculated with local-approximation model electron fluxes in Titan's atmosphere during the T40 flyby. The solid black line corresponds to the model results for the altitude shown in each panel. The unidirectional fluxes calculated by the local model are divided by  $4\pi$  in order to compare with the measured differential fluxes. The blue and red lines correspond to the average measured fluxes for the ingress and egress parts of the flyby. The averaging is performed by the combination of all available measured spectra  $\pm 5$  km from the reference altitude. The available number of spectra is given in each panel. The error bars correspond to the uncertainty of the averaged spectra assuming Poisson statistics. The dashed line corresponds to the one count level converted to differential flux. (For interpretation of the references to color in this figure legend, the reader is referred to the web version of this article.)

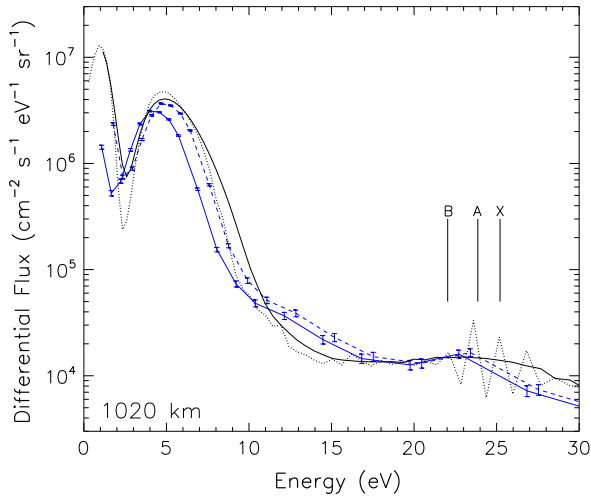


**Fig. 8.** Comparison among measured and calculated differential fluxes at 1020 km. The dotted and solid lines correspond to the model results for the high resolution energy spectrum and the calculated spectrum convolved to the CAPS energy resolution. The lines with error bars correspond to the measurements assuming a spacecraft potential of  $-0.5$  eV (solid line) and  $-1.2$  eV (dashed line). The three vertical lines mark the energy of photoelectrons produced by the photoionization of  $N_2$  in the X, A and B states.

ger flux of electrons that is decreasing rather slowly with increasing energy. It is interesting to note that the structure of the observed high energy fluxes is very similar to the variation implied by a constant count rate of 1 Hz. Thus, this part of the observations appears to be an instrument artifact (see also Arridge et al., 2009). A contribution of magnetospheric electrons could also affect the measurements in this energy range, but there is no reason why this would be parallel to the instrument response curve.

For the lower energies measured by CAPS ( $E < 5$  eV) the most prominent feature observed is the maximum between 4 and 5 eV. The location of the nearby minimum based on the model results should be at 2.3 eV but the observations suggest a minimum at a slightly smaller energy. In addition the magnitude of the flux is different between the model and the observations between the peak and the trough, especially with increasing altitude. The first discrepancy is related to the value of the spacecraft potential used in the retrieval of the electron fluxes. The results presented in Fig. 7 assume a  $-0.5$  eV for the spacecraft potential but close inspection of the location of the HeII photoelectron peak suggest a larger value which would bring the location of the minimum in the low energy in good agreement with the observations. This is demonstrated in Fig. 8, where the retrieved differential flux assuming a spacecraft potential of  $-1.2$  eV is compared with the observations (for more details in the spacecraft potential see Lewis et al., 2010). The depth of the minimum is affected by plasma instabilities related to the shape of the suprathermal electron distribution (Galand et al., 2006 and references therein). This has been observed in Earth's atmosphere as well, but no rigorous correction method has been determined so far. Thus, in the energy range where the observations are reliable, the model appears to be in good agreement with them.

#### 4.2. EUV/FUV emissions

The Cassini UltraViolet Imaging Spectrometer (UVIS) provided measurements of the EUV and FUV emissions from Titan's disk (Ajello et al., 2007, 2008). The published emissions are from the second Titan flyby (TB) on December 13th, 2004. We compare the observed emissions with our model results for a solar zenith

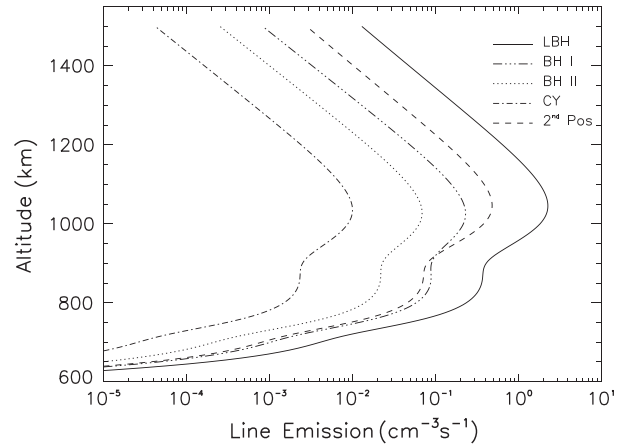


**Fig. 9.** Volume emission at different bands of  $N_2$  due to suprathermal electron impact.

angle of  $60^\circ$ , which is closest to the disk average observations. For the case of suprathermal electron impact, the volume emission rate for each line, at each altitude,  $P_\lambda(z)$ , is calculated from:

$$P_\lambda(z) = \int \Phi(z, E) \sigma_\lambda^{em}(E) n(z) dE \quad (11)$$

with  $\Phi(z, E)$  the electron flux at energy  $E$  and altitude  $z$ ,  $\sigma_\lambda^{em}$  the emission cross section at wavelength  $\lambda$  for electron impact at energy  $E$ , and  $n(z)$  the  $N_2$  number density. The peak emission from electron excitation is located close to 1000 km, thus, we can use the local approximation model for these calculations. A similar expression is used for the volume emission rates by photon induced transitions. The emission cross sections used in the calculations are described in Appendix B.

Some of the lines observed by UVIS are generated by both photoabsorption and electron impact, while others are specific to the processes generating them. Fig. 9 presents the volume emission rates from different excited states of  $N_2^+$  due to electron impact under solar illumination. The dominant emission from the optically forbidden LBH band ( $\alpha^1\Pi_g \rightarrow X^1\Sigma_g^+$ ) is located in the FUV region, while the other bands are observed in the EUV region. The altitude dependence of the rates reflects the electron production rates described above, with a peak just above 1000 km from the production of primary photoelectrons and a shoulder close to 800 km due to secondary electron production. The corresponding volume emission rates from the excited dissociation fragments of  $N_2$  ( $N^*$  and  $N^{+*}$ ) are presented in Fig. 10 for both photo and electron-induced transitions, with the former having a significantly larger contribution than the latter.

The emission observed by UVIS corresponds to the integrated volume emission along the line of sight. They correspond to measurements of Titan's disk, thus we calculated the model intensity for nadir viewing, taking into account the attenuation of the emitted photons by  $N_2$  and  $CH_4$  absorption. The resulting FUV intensities are presented in Table 4 and compared with the observations. Considering that the calculated emissions are an upper limit, due to the specific nadir viewing relative to the disk average UVIS observations and also due to the local approximation for the suprathermal electrons calculations, there is a very good agreement between observations and experiment. We note also that for increasing wavelengths of emitted radiation, the agreement becomes better because the attenuation due to atmospheric absorption becomes smaller. The emissions at the EUV regions from the excited  $N_2^+$  states are subject to multiple scattering of the Carroll–Yoshino band ( $c_4^1\Sigma_u^+ \rightarrow X^1\Sigma_g^+$ ) and requires more compli-

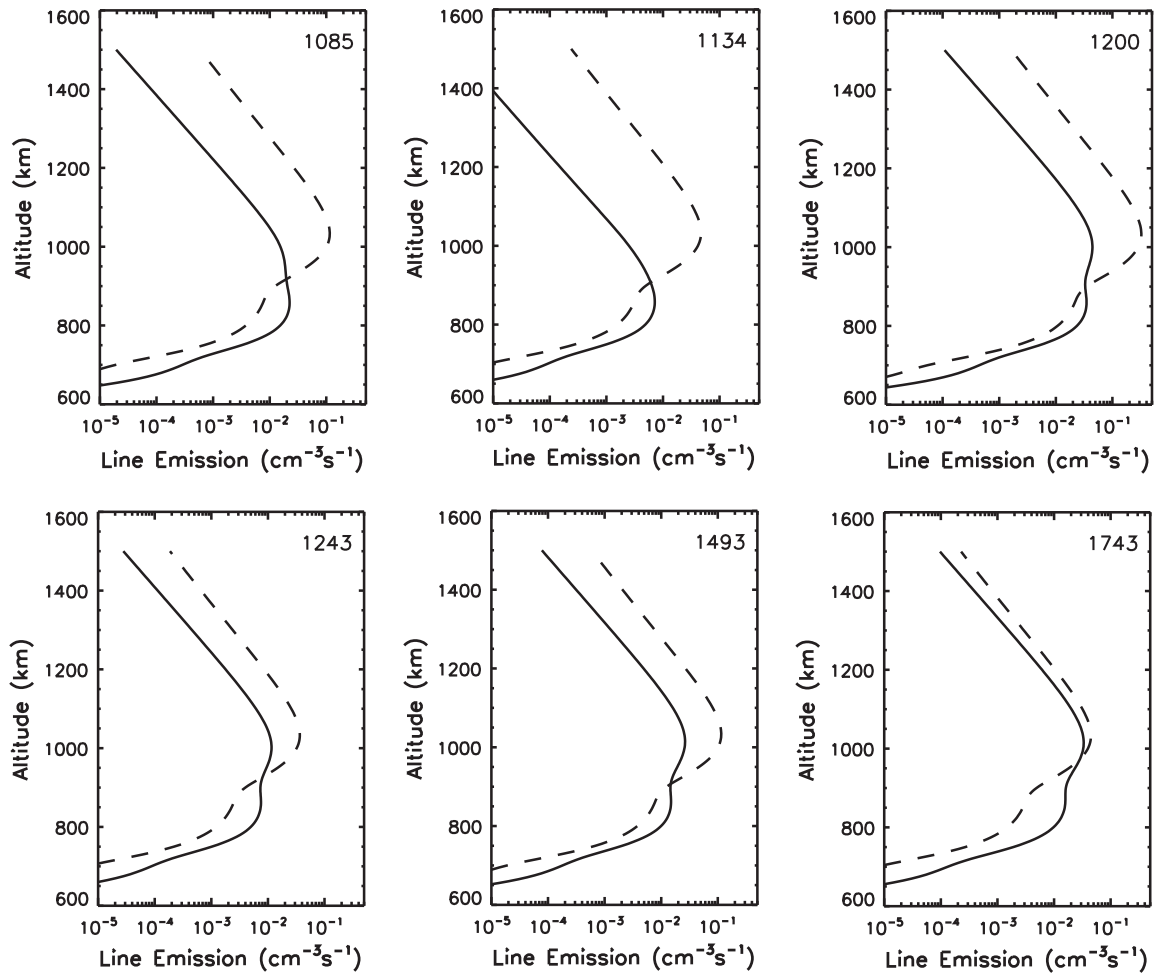


Fig. 10. Volume emission by atomic N and N<sup>+</sup> at the designated wavelengths (in Å) induced by photons (dashed line) and suprathermal electrons (solid line).

cated calculations (Stevens, 2001; Ajello et al., 2007). These are beyond the scope of the current work where we only attempt to validate our model calculations.

Thus, the validation of the model calculations against both the UVIS and CAPS observations confirms an accurate reproduction of the energetic processes in Titan's upper atmosphere.

## 5. Chemical production rates

Identification of the initial photolysis products and the rate at which they are generated in the atmosphere is imperative in order to have a correct description of the subsequent chemistry. For disk average calculations (SZA = 60°) the resulting production rates of radicals and ions from photon and photoelectron impact on N<sub>2</sub> and CH<sub>4</sub> are presented in Fig. 11. We note here that our results correspond to diurnal averages, which means that the daytime calculations have been multiplied by 1/2.

For molecular nitrogen, photons have a peak contribution at ~1000 km (Fig. 11a), while the contribution of suprathermal electrons becomes dominant between 700 and 900 km due to the production of secondary electrons in this area by the solar soft X-rays (Fig. 11b). Thus, both dissociation sources are required for the description of the total N<sub>2</sub> loss rate (Fig. 11c). Based on our calculations, the total column destruction rate of N<sub>2</sub> by photons is  $2.77 \times 10^8 \text{ cm}^{-2} \text{ s}^{-1}$  (all column values are referred to the surface). The photoionization of N<sub>2</sub> accounts for 67% of this rate ( $1.85 \times 10^8 \text{ cm}^{-2} \text{ s}^{-1}$ ), while the rest of the loss rate is approximately equally divided between dissociative photoionization

( $4.57 \times 10^7 \text{ cm}^{-2} \text{ s}^{-1}$ ) and neutral photodissociation ( $4.61 \times 10^7 \text{ cm}^{-2} \text{ s}^{-1}$ ). For electron impact the total column loss is  $1.6 \times 10^8 \text{ cm}^{-2} \text{ s}^{-1}$ , with 66.9% corresponding to N<sub>2</sub><sup>+</sup> formation ( $1.07 \times 10^8 \text{ cm}^{-2} \text{ s}^{-1}$ ), 24.6% to neutral dissociation ( $3.93 \times 10^7 \text{ cm}^{-2} \text{ s}^{-1}$ ) and 8.5% to dissociative ionization ( $1.36 \times 10^7 \text{ cm}^{-2} \text{ s}^{-1}$ ).

Our calculations show that the use of the high spectral resolution cross section, along with a high resolution solar spectrum, provides a significantly different photolysis profile than the results obtained with low resolution parameters (Fig. 12). The highly structured cross sections above 800 Å allow for less absorption to

Table 4

Comparison between calculated and observed emissions from Titan's disk. The wavelengths for which results are provided are not affected by multiple scattering and the impact of atmospheric attenuation by N<sub>2</sub> and CH<sub>4</sub> is taken into account. The individual contribution of photons (Ph) and electrons (El) in the calculations are reported, while the observed emissions with uncertainty, when available, are taken from Ajello et al. (2007, 2008). All values are in Rayleigh.

| Band/line (Å)   | Model |       |       | UVIS (Rayleigh) |
|-----------------|-------|-------|-------|-----------------|
|                 | Ph    | El    | Total |                 |
| 1085            | 1.92  | 0.35  | 2.27  | 2.31            |
| 1135            | 0.88  | 0.09  | 0.96  | 1.33            |
| 1200            | 6.62  | 1.03  | 7.65  | 6.8             |
| 1243            | 0.75  | 0.26  | 1.01  | 0.6             |
| 1493            | 2.35  | 0.73  | 3.08  | 3.0             |
| 1743            | 0.90  | 0.87  | 1.77  | 1.6             |
| Total NI        | 14.70 | 3.64  | 18.34 | 16              |
| LBH (1250–2600) | –     | 41.24 | 41.24 | 43 ± 7          |

take place at any altitude, compared to the resulting absorption when a low-resolution cross section is used. In other words the absorption by  $N_2$  is spread over a larger altitude range. This affects the methane photoabsorption because its cross section does not exhibit such a highly variable structure. As a result, photons not absorbed by  $N_2$  at a specific altitude are absorbed by  $CH_4$ , leading to a lower destruction for  $N_2$  and a higher destruction rate for  $CH_4$ , relative to the rates calculated assuming a low-resolution cross section for nitrogen (Fig. 12).

We get a different picture for the altitude dependence of the destruction rates of methane because its absorption spectrum extends to longer wavelengths than that of  $N_2$ . Ionization by photons peaks at 1000 km, similar to  $N_2$ , but neutral dissociation by photons extends to lower altitudes with a maximum at  $\sim 800$  km (Fig. 11d). Photoelectrons dissociate methane at 1000 km (primary

electrons) and at 700–900 km (secondary electrons), providing a significant ion production in the latter region, but do not significantly affect the total production of neutral fragments (Fig. 11e and f). The column integrated loss rate of methane due to photons is  $3.08 \times 10^9 \text{ cm}^{-2} \text{ s}^{-1}$ , which is dominated by neutral dissociation; the photoionization accounts to  $3.22 \times 10^7 \text{ cm}^{-2} \text{ s}^{-1}$ . The impact of suprathermal electrons provides a column loss of  $2.69 \times 10^7 \text{ cm}^{-2} \text{ s}^{-1}$  with 53.4% corresponding to neutral dissociation and the rest to ionization.

The impact of the high-resolution cross section of  $N_2$  is more prominent in the case of  $CH_4^+$  production. The cross sections for the production of  $CH_3^+$  and  $CH_4^+$  are identical apart from their extent to the low energy region (see Fig. 4). The  $CH_4^+$  threshold is at 983 Å, while the  $CH_3^+$  threshold is at 870 Å. As a result  $CH_4^+$  production is significantly affected by the use of the high-resolution

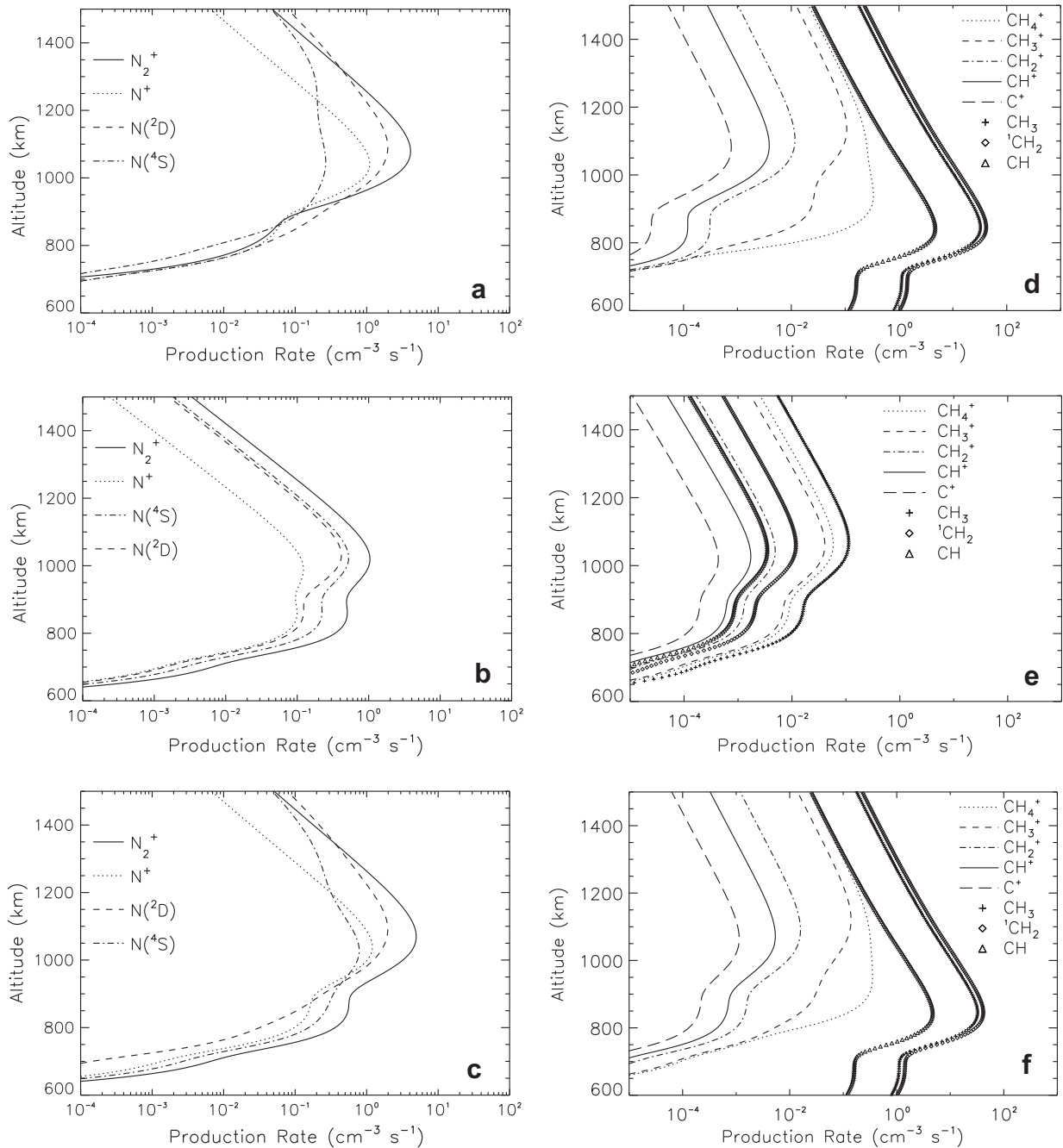


**Fig. 11.** Productions rates of different dissociation products of  $N_2$  and  $CH_4$  due to photons (top row), suprathermal electrons (middle row) and cumulative (bottom row). Note that the profiles have been multiplied by half in order to take into account the day length.

nitrogen cross sections, since photons experiencing a smaller absorption by  $N_2$  in this spectral region, are able to penetrate deeper in the atmosphere and ionize methane to  $CH_4^+$  at lower altitudes close to 800 km (see Fig. 11d). For  $CH_3^+$  though, which does not have significant cross section at this spectral region the production has its peak at a higher altitude, close to 1000 km. The column production rates for each radical/ion produced are presented in Table 5.

The above results are not altered if the contribution of isotopic nitrogen is taken into account. Isotopic substitution results in small shifts in the rotational and vibrational levels of the molecules, which translates to small shifts in their photoabsorption cross sections. Thus, the presence of  $^{15}N^{14}N$  in Titan's atmosphere could affect the penetration altitude of photons in the highly structured spectral region of neutral dissociation. We included  $^{15}N^{14}N$  in our calculations with an isotopic ratio of 183, measured in the lower atmosphere by the Cassini Gas Chromatographer Mass Spectrometer (GCMS) (Niemann et al., 2005). Although in the upper atmosphere, where  $N_2$  is photolyzed, the isotopic ratio will increase due to diffusive separation we use this value as an upper limit of the isotopic opacity contribution. The theoretical calculations presented above also provide high-resolution cross sections for isotopic nitrogen, which we used for the simulation. Our results suggest that the impact in the photolysis rates of  $N_2$  and  $CH_4$  is negligible, although the photolysis rate ( $J$  value) of isotopic nitrogen is 30 times larger than the corresponding value for  $N_2$  at the photolysis peak. This is similar to the results of Liang et al. (2007) for the photolysis rate of isotopic nitrogen.

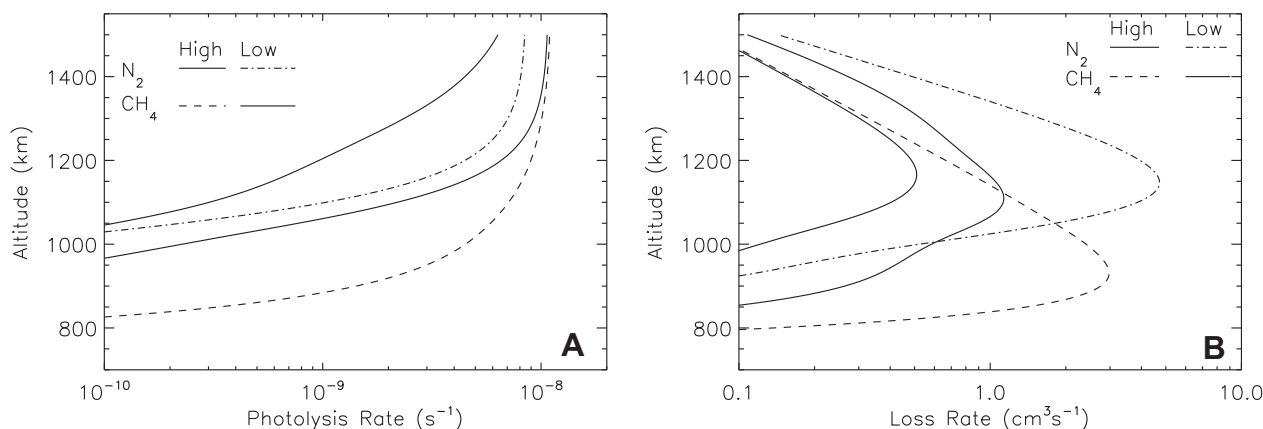


**Fig. 12.** Photolysis and loss rates of  $N_2$  and  $CH_4$  for the high (solid line for  $N_2$  and dashed line for  $CH_4$ ) and low resolution (dash-dotted line for  $N_2$  and dash-triple-dotted line for  $CH_4$ ) cross sections of molecular nitrogen in the spectral region between 800 and 1000 Å. The solar zenith angle for these calculations is 60°. No diurnal averaging has been included.

**Table 5**

Column production rates for each fragment of the dissociation of  $N_2$  and  $CH_4$  from photons (P) and photoelectrons (PE) at 60° solar zenith angle and total column production at different solar zenith angles. Values are given in  $cm^{-2} s^{-1}$  scaled to the surface. Day length scaling has been taken into account.  $^1CH_2$  correspond to the first excited state of methylene ( $\alpha^1A_1$ ). Read a(b) as  $a \times 10^b$ .

| SZAs<br>product | 60°     |         |         | 0°      | 15°     | 30°     | 45°     | 50°     | 75°     |
|-----------------|---------|---------|---------|---------|---------|---------|---------|---------|---------|
|                 | P       | PE      | Total   |         |         |         |         |         |         |
| $N_2^+$         | 1.85(8) | 1.07(8) | 2.92(8) | 5.50(8) | 5.33(8) | 4.81(8) | 3.98(8) | 3.65(8) | 1.72(8) |
| $N^+$           | 4.57(7) | 1.36(7) | 5.93(7) | 1.11(8) | 1.08(8) | 9.73(7) | 8.07(7) | 7.41(7) | 3.52(7) |
| $N(^4S)$        | 2.41(7) | 5.29(7) | 7.70(7) | 1.50(8) | 1.45(8) | 1.30(8) | 1.07(8) | 9.77(7) | 4.30(7) |
| $N(^2D)$        | 1.13(8) | 3.93(7) | 1.53(8) | 2.95(8) | 2.85(8) | 2.56(8) | 2.11(8) | 1.93(8) | 8.66(7) |
| $CH_4^+$        | 2.32(7) | 6.64(6) | 2.98(7) | 5.14(7) | 5.00(7) | 4.58(7) | 3.90(7) | 3.62(7) | 1.84(7) |
| $CH_3^+$        | 7.07(6) | 4.65(6) | 1.17(7) | 1.83(7) | 1.78(7) | 1.66(7) | 1.46(7) | 1.37(7) | 8.08(6) |
| $CH_2^+$        | 6.88(5) | 5.65(5) | 1.25(6) | 1.91(6) | 1.87(6) | 1.75(6) | 1.54(6) | 1.45(6) | 8.86(5) |
| $CH^+$          | 2.18(5) | 1.99(5) | 4.18(5) | 6.40(5) | 6.26(5) | 5.83(5) | 5.14(5) | 4.85(5) | 2.95(5) |
| $C^+$           | 4.28(4) | 5.08(4) | 9.36(4) | 1.45(5) | 1.41(5) | 1.32(5) | 1.16(5) | 1.09(5) | 6.58(4) |
| $CH_3$          | 1.25(9) | 1.29(7) | 1.26(9) | 2.35(9) | 2.28(9) | 2.06(9) | 1.71(9) | 1.57(9) | 7.67(8) |
| $^1CH_2$        | 1.61(9) | 1.37(6) | 1.62(9) | 3.02(9) | 2.92(9) | 2.63(9) | 2.19(9) | 2.01(9) | 9.80(8) |
| CH              | 1.83(8) | 4.05(5) | 1.83(8) | 3.42(8) | 3.31(8) | 2.99(8) | 2.48(8) | 2.28(8) | 1.11(8) |

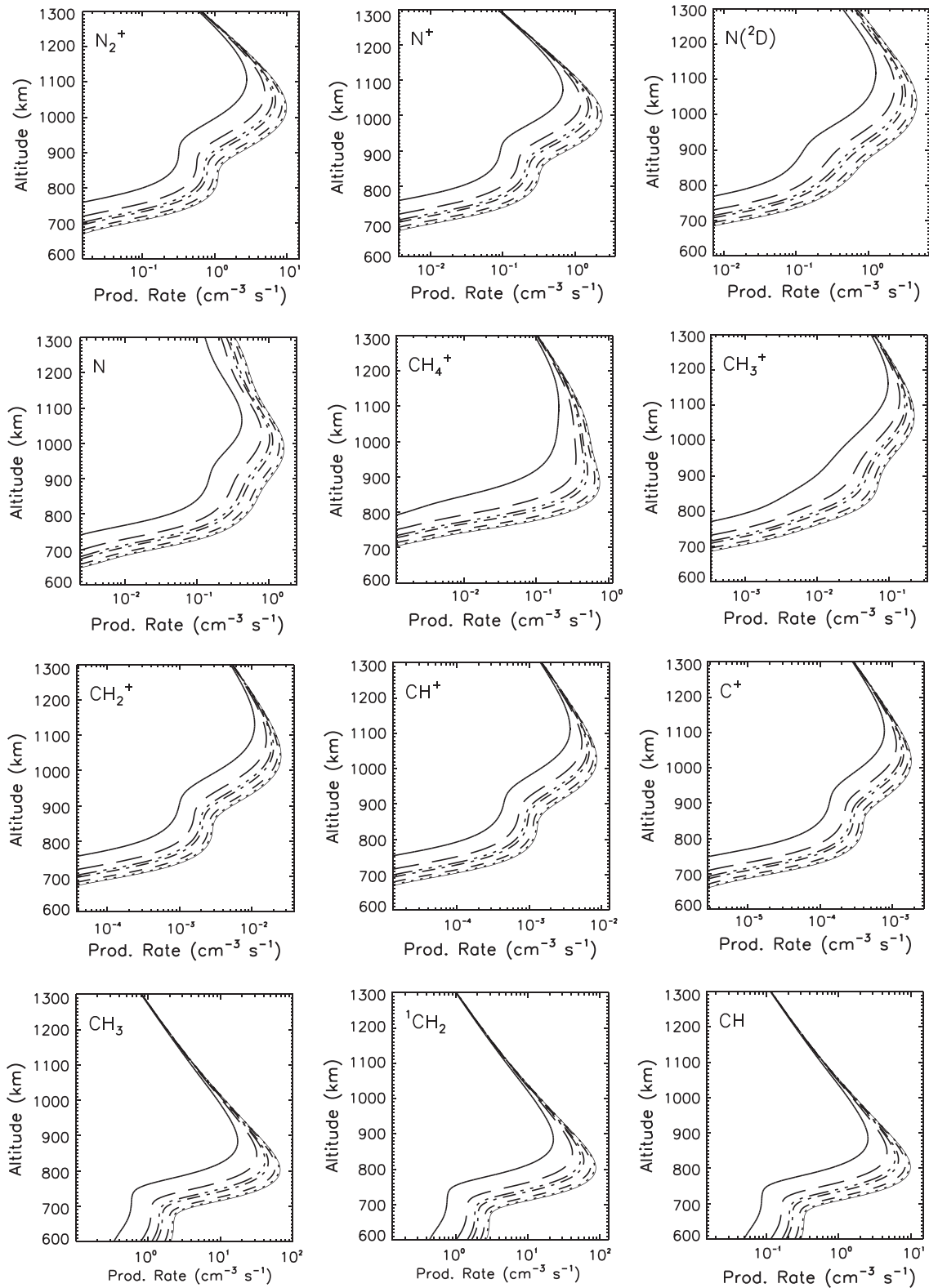


**Fig. 13.** Production profiles for different product of  $N_2$  and  $CH_4$  photolysis at different solar zenith angles (ZA). The profiles include the contributions from both photons and suprathermal electrons. Different curves correspond to different ZA:  $0^\circ$  thin solid line,  $15^\circ$  dotted line,  $30^\circ$  dashed line,  $45^\circ$  dash-dotted line,  $50^\circ$  dash-triple-dotted line,  $60^\circ$  long-dashed line and  $70^\circ$  thick solid line.

should note that their resulting photodissociation rate for wavelengths between 800 and 1000 Å has a different altitude structure than ours (Fig. 12). We believe this is due to the spectral range over which the high-resolution cross sections are used. Liang et al. (2007) use these between 827 and 1000 Å, while in our calculations

we set the lower boundary at 845 Å based on the comparison of the theoretical cross sections with laboratory measurements (see Fig. 2 and discussion above). As a result more photons in our calculations are deposited close to 1100 km relative to Liang et al. (2007). We should note that between 830 and 840 Å the solar

**Table 6**Comparison of N<sub>2</sub> loss rates among different photochemical models. See text for details.

| Reaction  | Current work | Krasnopolsky (2009) | Lavvas et al. (2008b) | Wilson and Atreya (2004)                    |
|---|--------------|---------------------|-----------------------|---|
| N <sub>2</sub> + hν → N( <sup>2</sup> D) + N( <sup>2</sup> D) | 2.52(7)      | –                   | –                     | –   |
| N + N( <sup>2</sup> D)  | 2.09(7)      | 9.01(7)             | 1.5(8)                | ~8.3(7) (total neutral)                     |
| N <sub>2</sub> <sup>+</sup> + e                               | 1.85(8)      | 2.19(8)             | 2.05(8)               | 1.6(8) (total N <sub>2</sub> <sup>+</sup> ) |
| N/N( <sup>2</sup> D) + N <sup>+</sup>                         | 4.57(7)      | 5.49(7)             | 5.34(7)               | 4.7(7) (total N <sup>+</sup> )              |
| N <sub>2</sub> + e → N + N( <sup>2</sup> D) + e               | 3.93(7)      | 1.1(8)              | –                     | –   |
| N <sub>2</sub> <sup>+</sup> + e + e                           | 1.07(8)      | –                   | –                     | –   |
| N <sup>+</sup> + N/N( <sup>2</sup> D) + e + e                 | 1.36(7)      | –                   | –                     | –   |
| Total N <sub>2</sub> loss                                     | 4.37(8)      | 4.74(8)             | 4.08(8)               | 2.9(8)                                      |

**Table 7**Products and threshold energies for electron impact on N<sub>2</sub> and CH<sub>4</sub>.

| N <sub>2</sub> state   | Threshold               | Products                                | CH <sub>4</sub> state | Threshold | Product  |
|--|-------------------------|---|-----------------------|-----------|--|
| N <sub>2</sub> Rotj = 0 → 2  | 1.48 × 10 <sup>-3</sup> | N <sub>2</sub> <sup>+</sup>             | Vib 2–4               | 0.162     | CH <sub>4</sub> <sup>+</sup>                       |
| N <sub>2</sub> Vibv = 0 → 1  | 0.289                   | N <sub>2</sub>                          | Vib 1–3               | 0.361     | CH <sub>4</sub> <sup>+</sup>                       |
| N <sub>2</sub> A <sup>3</sup> Σ <sub>u</sub> <sup>+</sup>              | 6.169                   | N <sub>2</sub>                          | Dis                   | 7.5       | CH <sub>3</sub> + H                                |
| N <sub>2</sub> B <sup>3</sup> Π <sub>g</sub>                           | 7.353                   | N <sub>2</sub>                          | Dis                   | 8.5       | <sup>1</sup> CH <sub>2</sub> + 2H                  |
| N <sub>2</sub> W <sup>3</sup> Δ <sub>u</sub>                           | 7.362                   | N <sub>2</sub>                          | Dis                   | 15.5      | CH + H <sub>2</sub> + H                            |
| N <sub>2</sub> B <sup>3</sup> Σ <sub>u</sub> <sup>-</sup>              | 8.165                   | N <sub>2</sub>                          | Ion                   | 13.844    | CH <sub>4</sub> <sup>+</sup> + e                   |
| N <sub>2</sub> α <sup>1</sup> Σ <sub>u</sub> <sup>-</sup>              | 8.399                   | N <sub>2</sub>                          | Ion                   | 14.323    | CH <sub>3</sub> <sup>+</sup> + H + e               |
| N <sub>2</sub> α <sup>1</sup> Π <sub>g</sub>                           | 8.549                   | N <sub>2</sub>                          | Ion                   | 19.890    | CH <sub>3</sub> <sup>+</sup> + H + 2e              |
| N <sub>2</sub> w <sup>1</sup> Δ <sub>u</sub>                           | 8.890                   | N <sub>2</sub>                          | Ion                   | 21.11     | CH <sub>3</sub> <sup>+</sup> + H + 2e              |
| N <sub>2</sub> C <sup>3</sup> Π <sub>u</sub>                           | 11.032                  | N( <sup>2</sup> D) + N( <sup>4</sup> S) | Ion                   | 15.21     | CH <sub>2</sub> <sup>+</sup> + 2H + 2e             |
| N <sub>2</sub> E <sup>3</sup> Σ <sub>g</sub> <sup>+</sup>              | 11.875                  | N( <sup>2</sup> D) + N( <sup>4</sup> S) | Ion                   | 19.89     | CH <sub>2</sub> <sup>+</sup> + 2H + 2e             |
| N <sub>2</sub> α <sup>1</sup> Σ <sub>g</sub> <sup>+</sup>              | 12.255                  | N( <sup>2</sup> D) + N( <sup>4</sup> S) | Ion                   | 21.11     | CH <sub>2</sub> <sup>+</sup> + 2H + 2e             |
| N <sub>2</sub> b <sup>1</sup> Π <sub>u</sub>                           | 12.500                  | N( <sup>2</sup> D) + N( <sup>4</sup> S) | Ion                   | 22.41     | CH <sub>2</sub> <sup>+</sup> + 2H + 2e             |
| N <sub>2</sub> b <sup>1</sup> Σ <sub>u</sub>                           | 12.854                  | N( <sup>2</sup> D) + N( <sup>4</sup> S) | Ion                   | 28.20     | CH <sub>2</sub> <sup>+</sup> + 2H + 2e             |
| N <sub>2</sub> c <sub>4</sub> <sup>1</sup> Σ <sub>u</sub> <sup>+</sup> | 12.935                  | N( <sup>2</sup> D) + N( <sup>4</sup> S) | Ion                   | 22.60     | CH <sup>+</sup> + H <sub>2</sub> + H + 2e          |
| N <sub>2</sub> <sup>+</sup> X <sup>2</sup> Σ <sub>g</sub> <sup>+</sup> | 15.581                  | N <sup>+</sup> + N( <sup>4</sup> S)     | Ion                   | 28.50     | CH <sup>+</sup> + H <sub>2</sub> + H + 2e          |
| N <sub>2</sub> <sup>+</sup> A <sup>2</sup> Π <sub>g</sub>              | 16.699                  | N <sup>+</sup> + N( <sup>4</sup> S)     | Ion                   | 27.00     | CH <sup>+</sup> + H <sub>2</sub> + H + 2e          |
| N <sub>2</sub> <sup>+</sup> B <sup>2</sup> Σ <sub>u</sub> <sup>+</sup> | 18.751                  | N <sup>+</sup> + N( <sup>4</sup> S)     | Ion                   | 23.53     | H <sub>2</sub> <sup>+</sup> + CH <sub>2</sub> + 2e |
|  |                         |   | Ion                   | 28.90     | H <sub>2</sub> <sup>+</sup> + CH <sub>2</sub> + 2e |
|  |                         |   | Ion                   | 23.70     | H <sup>+</sup> + CH <sub>3</sub> + 2e              |
|  |                         |   | Ion                   | 27.50     | H <sup>+</sup> + CH <sub>3</sub> + 2e              |

spectrum has a strong emission feature. Thus, detailed knowledge of the N<sub>2</sub> cross section in this region is necessary in order to constrain the altitude penetration of these photons. The use of different cross sections is also reflected in the total N<sub>2</sub> photoabsorption rate, which for Liang et al. (2007) is  $1.9 \times 10^8 \text{ cm}^{-2} \text{ s}^{-1}$  compared to  $2.77 \times 10^8 \text{ cm}^{-2} \text{ s}^{-1}$  in our calculations. On the other hand, Liang et al. (2007) suggest that the total atomic nitrogen input at the top of the atmosphere is in the range  $(1\text{--}2) \times 10^9 \text{ cm}^{-2} \text{ s}^{-1}$  based on Voyager estimations for the contribution of magnetospheric electrons and cosmic rays. GCR deposit their energy in the stratosphere therefore should not be considered as a source of atomic N in the upper atmosphere, while their column integrated production of N is in the order of  $10^8 \text{ cm}^{-2} \text{ s}^{-1}$  (Molina-Cuberos et al., 1999). Furthermore, in view of our analysis and the small contribution of magnetospheric electrons this estimation also appears too large.

We have also presented a model for the energy degradation of photoelectrons in Titan's atmosphere based on the local deposition approximation. The consistency of our results with the detailed transport calculations suggests that this approximation, can be applied safely at altitudes below 1200 km but this transition region can vary with the solar zenith angle. Our simulation of the photon and photoelectron interaction with the main species of Titan's atmosphere reproduces very well the observed dayside electron fluxes and EUV/FUV emissions measured by the Cassini CAPS/ELS and UVIS instruments, respectively.

On the nightside of Titan's atmosphere, energy is provided mainly through the magnetospheric electrons. From the so far observations, the contribution of magnetospheric electrons in the energetic electron fluxes is small. The TB flyby observations did not detect any nighttime EUV emissions related to atmospheric

processes (Ajello et al., 2007), while the FUV emissions indicated a H Ly-α emission along with weak N emission, without any detectable contribution from the LBH band (Ajello et al., 2008), which is generated only by electron impact. In other flybys, nighttime EUV emissions are present while FUV emissions range up to 50% of the corresponding daytime emissions. Similarly, CAPS/ELS spectra from Titan's nightside during flybys T5 and T21 (Cravens et al., 2009) are variable and at least an order of magnitude lower than the corresponding spectra at similar altitudes of the day side, as reported here and also in Galand et al. (2010). Thus, the contribution of magnetospheric electrons always appears to have a smaller contribution than photons. Similarly, the contribution of magnetospheric energetic ions is inferred to be small under typical Titan conditions (Cravens et al., 2008; Sittler et al., 2009), thus was not included in our calculations. During high magnetospheric activity periods, such as those observed during the T5 flyby, the contribution of energetic ions could be comparable with the ionization rates by solar photons. Yet, the observations so far suggest that these events are infrequent and thus cannot affect the photochemistry over long time scales.

The dominance of photons and photoelectrons over magnetospheric electrons and ions as energy sources in Titan's upper atmosphere, suggests that the former suffice for the description of the primary chemical precursors of the subsequent chemistry in the upper atmosphere. In addition to the calculated destruction rates for nitrogen and methane, the contribution from GCR must be included in order to provide a complete description of the radicals and ions produced. Due to their high energy, GCR are able to penetrate deep in the atmosphere (Capone et al., 1983; Borucki et al., 1987; Molina-Cuberos et al., 1999) and provide the only

means for braking  $N_2$  molecules in the stratosphere, enhancing the nitrogen chemistry at these altitudes (Molina-Cuberos et al., 1999, 2002; Lavvas et al., 2008b). The Huygens measurements for the conductivity of the lower atmosphere reveal a peak in the density of electrons and ions close to 65 km, consistent with the theoretical results (Lopez-Moreno et al., 2008). On the other hand, the positive (cations) and negative (anions and electrons) charged components demonstrate a different variation in their vertical density profiles. These differences are attributed to electron capture by aerosols (Lopez-Moreno et al., 2008). Thus, in order to quantify the impact of GCR in the lower atmosphere the current models must consider the inclusion of heterogeneous processes at the surface of aerosols.

Since we have validated rates for the primary products of Titan's upper atmosphere, we can compare our results with previous calculations that did not have the privilege of the Cassini measurements, presented here. We should note though, that a comparison between different models is not a straight forward procedure since apart from the different parameterizations of each, the different input conditions and also the limitations of each model, should be taken into account. Table 6 presents a comparison among the  $N_2$  loss rates calculated here for photons and photoelectrons and the corresponding rates from the models of Wilson and Atreya (2004), Lavvas et al. (2008b), Krasnopolsky (2009) when available.

Wilson and Atreya (2004) calculated photon deposition in their simulated atmosphere and used the electron deposition models of Gan et al. (1992) and Keller et al. (1992), which were based on the Voyager measurements for the photoelectrons and magnetospheric electrons respectively. Lavvas et al. (2008b) considered only the neutral atmospheric chemistry, thus did not include the contribution of energetic electrons in their calculations. Krasnopolsky (2009) included both photons and energetic electrons, but the contribution of the latter was based on empirical formulas and not calculated from the photon flux directly. Unfortunately, the published papers do not all provide information for each process considered, thus, we only present the available data. The values for the Wilson and Atreya (2004) model correspond to the total  $N_2^+$  and  $N^+$  by both photons and energetic electrons taken from their Table 7, while we derived their neutral dissociation rate based on the total  $N_2$  loss rate reported. Overall the models agree in the total column loss rates of  $N_2$  except for the Wilson and Atreya (2004) model. The total loss rate for  $N_2$  reported in Krasnopolsky (2009) is 8.5% larger than our value, while the corresponding rate in the Lavvas et al. (2008b) model is 6.6% smaller (Table 6). In Wilson and Atreya (2004), the suprathermal electron contribution is significantly smaller than photolysis and their total  $N_2$  loss rate is 33.6% smaller

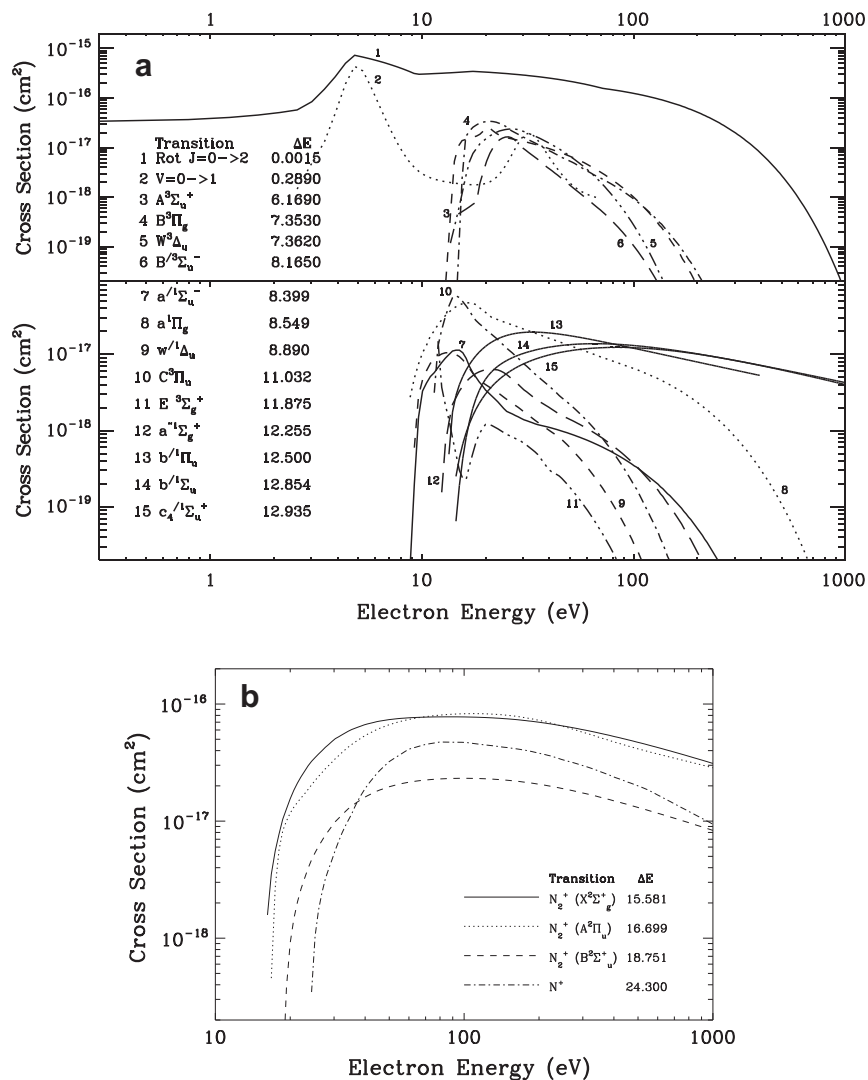


Fig. 14.  $N_2$  electron impact cross sections for excitation (upper panel) and ionization (lower panel). The possible transitions along with the threshold energy for each state are given.

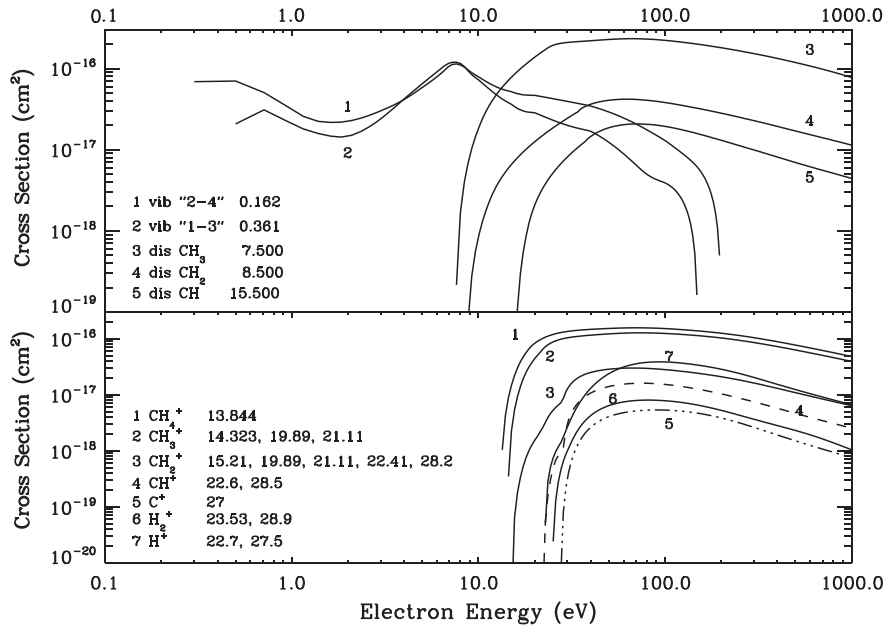
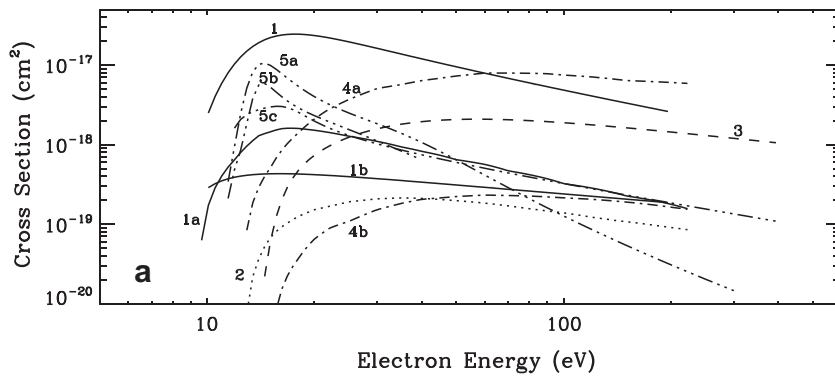


Fig. 15. CH<sub>4</sub> electron impact cross sections.



| Band Name                | Transition   | λ(A)   | key       |
|--------------------------|--|--------|-----------|
| Lyman-Birge-Hopfield     | α 'Π <sub>g</sub> → X 'Σ <sub>g</sub> <sup>+</sup>                             | Total  | 1200–2600 |
|                          |  | (3,3)  | 1493      |
|                          |  | (3,0)  | 1354      |
| Birge-Hopfield I         | b 'Π <sub>u</sub> → X 'Σ <sub>g</sub> <sup>+</sup>                             | (1,2)  | 1033      |
|                          |  | Total  | 857–945   |
| Birge-Hopfield II        | b' 'Σ <sub>u</sub> <sup>+</sup> → X 'Σ <sub>g</sub> <sup>+</sup>               | (0,0)  | 958       |
|                          |  | (16,0) | 871       |
| Carroll-Yoshino          | c <sub>4</sub> ' 'Σ <sub>u</sub> <sup>+</sup> → X 'Σ <sub>g</sub> <sup>+</sup> | (0,0)  | 3370      |
|                          |  | (1,0)  | 3158      |
|                          |  | (0,2)  | 3804      |
| 2 <sup>nd</sup> Positive | C 'Π <sub>g</sub> → A 'Σ <sub>g</sub> <sup>+</sup>                             | (0,0)  | 3370      |
|                          |  | (1,0)  | 3158      |
|                          |  | (0,2)  | 3804      |

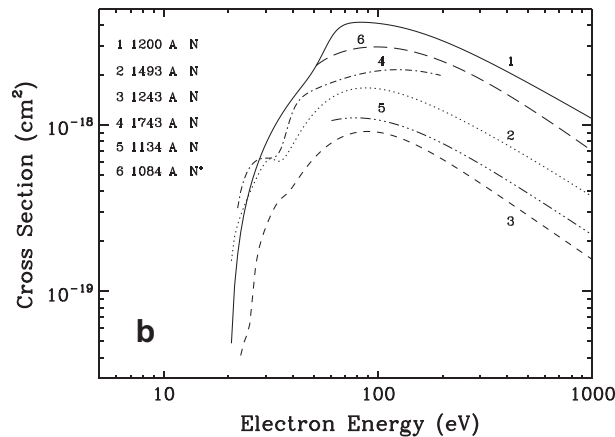


Fig. 16. Emission cross sections for photoelectron impact on N<sub>2</sub>. Upper panel is for de-excitation of N<sub>2</sub><sup>+</sup> states and lower panel for de-excitation of N and N<sup>+</sup> states.

ler than our result. The major differences among the models occur for the case of neutral photodissociation, which was not well constrained in the past, while the resulting rates of ionization and dissociative photoionization are in better agreement (Table 6). Although, we cannot directly compare our suprathreshold electrons calculations with previous model results due to the lack of information in them, we can note that the impact of this energy source is comparable with the photon contribution regarding the ionization of neutral  $N_2$  and should be included in calculations focusing in the investigation of the ion chemistry.

As explained above, the highly structured cross sections imply less  $N_2$  neutral photodissociation compared to previous calculations. Our result for the neutral dissociation rate of  $N_2$  is the smallest among the models ( $4.6 \times 10^7 \text{ cm}^{-2} \text{ s}^{-1}$ ), while the Krasnopolsky (2009) and Lavvas et al. (2008b) models are 95% and 225% higher, respectively. The value for the Wilson and Atreya (2004) model ( $8.3 \times 10^7 \text{ cm}^{-2} \text{ s}^{-1}$ ) corresponds to all loss processes but given the dominance of the photon contribution in their results (see their Fig. 17), it can be compared with our calculation. Also, it was a common approach in the past to consider production of N and  $N(^2D)$  products in equal amounts in the wavelength region 800–1000 Å. Our new scheme, presented above, allows also for the production of two excited nitrogen atoms. This yield is constrained to a narrow wavelength region between the ionization limit and 850 Å, but it overlaps with strong emission lines in the solar spectrum (Fig. 1) that enhance the  $N_2$  dissociation and the relative production of  $N(^2D)$ . Thus, although our total neutral dissociation is smaller than in previous calculations, the relative proportion of the highly reactive  $N(^2D)$  to the ground state  $N(^4S)$  is larger in our results. Due to its high reactivity relative to the ground state nitrogen, the  $N(^2D)$  production rate is an important parameter for the subsequent nitrogen chemistry in Titan's atmosphere. The overall  $N(^2D)$  production in our calculations from both photons and suprathreshold electrons is  $1.53 \times 10^8 \text{ cm}^{-2} \text{ s}^{-1}$ , which is very close to the value from Lavvas et al. (2008b) ( $1.5 \times 10^8 \text{ cm}^{-2} \text{ s}^{-1}$ ), although this model does not include the contribution of photoelectrons. Wilson and Atreya (2004) have a 45.8% smaller  $N(^2D)$  production rate, while Krasnopolsky (2009) have a 30.7% larger rate relative to our value. Photochemical models depend on a large number of parameters apart the photolysis rates, but given the above differences between the models used in the comparison of the  $N_2$  photolysis rates, divergences in the model results could result even if all other parameters were the same.

The above calculated rates along with the contribution of the galactic cosmic rays in the lower atmosphere are the basis for the photochemistry in Titan's atmosphere. We intend to update our photochemical calculations (Lavvas et al., 2008a,b; Vuitton et al., 2007; Horst et al., 2008; Yelle et al., 2010) with these results, along with the retrieved contribution from aerosols based on the DISR observations (Lavvas et al., 2010), in order to provide the most representative chemical structure of Titan's atmosphere.

## Acknowledgments

This work has been supported through NASA Grants NNX09AP14G and NNX09AB58G and NASA's Astrobiology Initiative through JPL subcontract 1372177 to the University of Arizona. M.G. was supported by the Science and Technology Facilities Council (STFC) rolling grant to Imperial College London. Development of the high-resolution  $N_2$  cross sections used in this work was supported by the Australian Research Council Discovery Program, through Grant Nos. DP0558962 and DP0773050.

## Appendix A. Electron impact

The electron impact cross sections for nitrogen and methane are presented in Figs. 14 and 15. The measurements for the cross sec-

tions of  $N_2$  are taken from the latest review of Itikawa (2006), which includes all the processes excited by electron impact (rotational, vibrational, electronic excitations, and ionization). The state specific ionization cross sections for  $N_2$  are taken from Shemansky and Liu (2005). The cross sections for methane are based on the electron impact ionization cross sections of Liu and Shemansky (2006) and the scaling law from the theoretical work of Erwin and Kunc (2005, 2008). The latter provides estimates for the electron impact dissociation cross sections of methane based on the measured cross sections for ionization. The cross sections for the vibrational excitation of methane are taken from Davies et al. (1989). The products of dissociation are summarized in Table 7.

## Appendix B. EUV and FUV emission

For Titan's atmosphere the EUV and FUV emissions observed are dominated by  $N_2$  features. Samson et al. (1991) and Meier et al. (1991) used synchrotron radiation to measure the  $N_2$  fluorescence at multiple wavelengths. They found that the observed emitted radiation originated from the de-excitation of excited N and  $N^+$  fragments produced by the dissociative photoionization of  $N_2$ . All of the emission lines were correlated with  $N_2$  excitation in the H band (see photoabsorption cross sections) which totally dissociates. Thus, it was possible to derive relative yields and emission cross sections for each line emission based on measured cross section for this band. This analysis assumes that there is no wavelength structure of the emission cross section relative to the H-band cross section. Also, emission at the observed wavelengths can also originate from neutral dissociation ( $N(^4S) + N^*$ ) or from higher excited states ( $N^{**} + N^*$  or  $N^{**} + N^+$ ) but these processes have very low efficiency and probability, respectively. Emissions at wavelengths beyond the detection limit of Meier et al. (1991) were also attributed to the same process. A complete list can be found in Bishop and Feldman (2003). Electron impact on  $N_2$  provides also significant UV emissions, some of them not allowed by photons such as the Lyman–Birge–Hopfield band. Reviews of emission cross sections for different transitions are reported in the literature (Itikawa, 2006; Tabata et al., 2006). A compilation of the cross sections used is presented in Fig. 16.

## References

- Agren, K., Wahlgund, J.-E., Garnier, P., Modolo, R., Cui, J., Galand, M., Muller-Wodarg, I., 2009. On the ionospheric structure of Titan. *Planet. Space Sci.* 57, 1821–1827.
- Ajello, J.M., Stevens, M.H., Stewart, I., Larsen, K., Esposito, L., Colwell, J., McClintock, W., Holsclaw, G., Gustin, J., Pryor, W., 2007. Titan airglow spectra from Cassini Ultraviolet Imaging Spectrograph (UVIS): EUV analysis. *Geophys. Res. Lett.* 34, L24202. doi:10.1029/2007GL031555.
- Ajello, J.M., Gustin, J., Stewart, I., Larsen, K., Esposito, L., Pryor, W., McClintock, W., Stevens, M.H., Malone, C.P., Dziczek, D., 2008. Titan airglow spectra from Cassini Ultraviolet Imaging Spectrograph: FUV analysis. *Geophys. Res. Lett.* 35, L06102. doi:10.1029/2007GL032315.
- Aoto, T., Ito, K., Hikosaka, Y., Shibasaki, A., Hirayama, R., Yamamoto, N., Miyoshi, E., 2006. Inner-valence states of  $N_2^+$  and the dissociation dynamics studied by threshold photoelectron spectroscopy and configuration interaction calculation. *J. Chem. Phys.* 124, 234306–234311.
- Arridge, C.S., Gilbert, L.K., Lewis, G.R., Sittler, E.C., Jones, G.H., Kataria, D.O., Coates, A.J., Young, D.T., 2009. The effect of spacecraft radiation sources on the electron moments from the Cassini CAPS electron spectrometer. *Planet. Space Sci.* 57, 854–869.
- Baltzer, P., Larsson, M., Karlsson, L., Wannberg, B., Carlsson Gothe, M., 1992. Inner-valence states of  $N_2^+$  studied by uv photoelectron spectroscopy and configuration–interaction calculations. *Phys. Rev. A* 46, 5545–5553.
- Bishop, J., Feldman, P.D., 2003. Analysis of the Astro-1/Hopkins Ultraviolet Telescope EUV–FUV dayside nadir spectral radiance measurements. *J. Geophys. Res.* 108, 1243. doi:10.1029/2001JA000330.
- Borucki, W.J., Levin, Z., Whitten, R.C., Keese, R.G., Capone, L.A., Summers, A.L., Toon, O.B., Dubach, J., 1987. Predictions of the electrical conductivity and charging of the aerosols in Titan's atmosphere. *Icarus* 72, 604–622.
- Capone, L.A., Dubach, J., Prasad, S.S., Whitten, R.C., 1983. Galactic cosmic rays and  $N_2$  dissociation in Titan. *Icarus* 55, 73–82.

- Carter, V.L., 1972. High-resolution N<sub>2</sub> absorption study from 730 to 980 Å. *J. Chem. Phys.* 56, 4195–4205.
- Cicerone, R.J., Swartz, W.E., Stolarski, R.S., Nagy, A.F., Nisbet, J.S., 1973. Thermalization and transport of photoelectrons: A comparison of theoretical approaches. *J. Geophys. Res.* 78, 6709–6728.
- Coates, A.J., Crary, F.J., Lewis, G.R., Young, D.T., Waite Jr., J.H., Sittler Jr., E.C., 2007. Discovery of heavy negative ions in Titan's ionosphere. *Geophys. Res. Lett.* 34, L22103. doi:10.1029/2007GL030978.
- Coates, A.J., Tsang, S.M.E., Wellbrock, A., Frahm, R.A., Winningham, J.D., Barabash, S., Lundin, R., Young, D.T., Crary, F.J., 2010. Ionospheric photoelectrons: Comparing Venus, Earth, Mars and Titan. *Planet. Space Sci.* doi:10.1016/j.pss.2010.07.016.
- Coustonis, A. et al., 2007. The composition of Titan's stratosphere from Cassini/CIRS mid-infrared spectra. *Icarus* 189, 35–62.
- Cravens, T.E., Robertson, I.P., Ledvina, S.A., Mitchell, D., Krimigis, S.M., Waite Jr., J.H., 2008. Energetic ion precipitation at Titan. *J. Geophys. Res. Lett.* 35, L03103. doi:10.1029/2007GL032451.
- Cravens, T.E. et al., 2009. Model-data comparisons for Titan's nightside ionosphere. *Icarus* 199, 174–188.
- Cui, J., Galand, M., Yelle, R.V., Vuitton, V., Wahlund, J.-E., Lavvas, P.P., Müller-Wodarg, I.C.F., Cravens, T.E., Kasprzak, W.T., Waite Jr., J.H., 2009. Diurnal variations of Titan's ionosphere. *J. Geophys. Res.* 114, A06310. doi:10.1029/2009JA014228.
- Davies, D.K., Kline, L.E., Bies, W.E., 1989. Measurements of swarm parameters and derived electron collision cross sections in methane. *J. Appl. Phys.* 65, 3311–3323.
- Erwin, D.A., Kunc, J.A., 2005. Electron-impact dissociation of the methane molecule into neutral fragments. *Phys. Rev. A* 72, 052719–052724.
- Erwin, D.A., Kunc, J.A., 2008. Dissociation and ionization of the methane molecule by nonrelativistic electrons including the near threshold region. *J. Appl. Phys.* 103, 064906–064914.
- Fennelly, J.A., Torr, D.G., 1992. Photoionization and photoabsorption cross sections of O, N<sub>2</sub>, O<sub>2</sub> and N for aeronomic calculations. *Atomic Data Nucl. Data Tabl.* 51, 321–363.
- Galand, M., Lilensten, J., Toublanc, D., Maurice, S., 1999. The ionosphere of Titan: Ideal diurnal and nocturnal cases. *Icarus* 140, 92–105.
- Galand, M., Yelle, R.V., Coates, A.J., Backes, H., Wahlund, J.E., 2006. Electron temperature of Titan's sunlit ionosphere. *Geophys. Res. Lett.* 33, L21101–L21105.
- Galand, M., Yelle, R., Cui, J., Wahlund, J.-E., Vuitton, V., Wellbrock, A., Coates, A., 2010. Ionization sources in Titan's deep ionosphere. *J. Geophys. Res.* 115. doi:10.1029/2009JA015100.
- Gan, L., Keller, C.N., Cravens, T.E., 1992. Electrons in the ionosphere of Titan. *J. Geophys. Res.* 97, 12137–12151.
- Havard, V.E., Lewis, B.R., Gibson, S.T., Stark, G., 2005. Rotational effects in the band oscillator strengths and predissociation linewidths for the lowest <sup>1</sup>Π<sub>u</sub> – X<sup>1</sup>Σ<sub>g</sub><sup>+</sup> transitions of N<sub>2</sub>. *J. Chem. Phys.* 123, 214304–214312.
- Herron, J.T., 1999. Evaluated chemical kinetics data for reactions of N(<sup>2</sup>D), N(<sup>2</sup>P) and N(<sup>4</sup>Σ<sub>g</sub><sup>+</sup>) in the gas phase. *J. Phys. Chem. Ref. Data* 28, 1453–1483.
- Horst, S., Vuitton, V., Yelle, R.V., 2008. The origin of oxygen species in Titan's atmosphere. *J. Geophys. Res.* doi:10.1029/2008JE00313.
- Itikawa, Y., 2006. Cross sections for electron collisions with nitrogen molecules. *J. Phys. Chem. Ref. Data* 35, 31–53.
- Kliore, A.J. et al., 2008. First results from the Cassini radio occultations of the Titan ionosphere. *J. Geophys. Res.* 113, 9317. doi:10.1029/2007JA012965.
- Krasnopolsky, V.A., 2009. A photochemical model of Titan's atmosphere and ionosphere. *Icarus* 201, 226–256.
- Krummacher, S., Schmidt, V., Wuilleumier, F., 1980. Inner-shell photoionization in molecules: The nitrogen case. *J. Phys. B* 13, 3993–4005.
- Keller, C.N., Cravens, T.E., Gan, L., 1992. A model of the ionosphere of Titan. *J. Geophys. Res.* 99, 6511–6525.
- Lavvas, P.P., Coustenis, A., Vardavas, I.M., 2008a. Coupling photochemistry with haze formation in Titan's atmosphere. Part I: Model description. *Planet. Space Sci.* 56, 27–66.
- Lavvas, P.P., Coustenis, A., Vardavas, I.M., 2008b. Coupling photochemistry with haze formation in Titan's atmosphere. Part II: Results and validation with Cassini/Huygens data. *Planet. Space Sci.* 56, 67–99.
- Lavvas, P., Yelle, R.V., Griffith, C.A., 2010. Titan's vertical aerosol structure at the Huygens landing site: Constraints on particle size, density, charge and refractive index. *Icarus* 210, 832–842.
- Lebonnois, S., Toublanc, D., 1999. Actinic fluxes in Titan's atmosphere, from one to three dimensions: Application to high-latitude composition. *J. Geophys. Res.* 104, 22025–22034.
- Lee, L.C., Chiang, C.C., 1983. Fluorescence yield from photodissociation of CH<sub>4</sub> at 1060–1420 Å. *J. Chem. Phys.* 78, 688–691.
- Lewis, B.R., Heays, A.N., Gibson, S.T., Lefebvre-Brion, H., Lefebvre, R., 2008a. A coupled-channel model of the <sup>3</sup>Π<sub>u</sub> states of N<sub>2</sub>: Structure and interactions of the 3σ<sub>g</sub>3<sup>3</sup>Π<sub>u</sub> and 3π<sub>u</sub>G<sub>3</sub><sup>3</sup>Π<sub>u</sub> Rydberg states. *J. Chem. Phys.* 129, 164306–164315.
- Lewis, B.R., Baldwin, K.G.H., Heays, A.N., Gibson, S.T., Sprengers, J.P., Ubachs, W., Fujitake, M., 2008b. Structure and predissociation of the 3pσ<sub>u</sub>D<sup>3</sup>Σ<sub>u</sub><sup>+</sup> Rydberg state of N<sub>2</sub>: First extreme-ultraviolet and new near-infrared observations, with coupled-channels analysis. *J. Chem. Phys.* 129, 204303–204314.
- Lewis, B.R., Gibson, S.T., Zhang, W., Lefebvre-Brion, H., Robbe, J.-M., 2005. Predissociation mechanism for the lowest <sup>1</sup>Π<sub>u</sub> states of N<sub>2</sub>. *J. Chem. Phys.* 122, 144302–144311.
- Lewis, G.R. et al., 2010. The calibration of the Cassini–Huygens CAPS electron spectrometer. *Planet. Space Sci.* 58, 427–436.
- Liang, M.-C., Heays, A.N., Lewis, B.R., Gibson, S.T., Yung, Y.L., 2007. Source of nitrogen isotope anomaly in HCN in the atmosphere of Titan. *Astrophys. J.* 664, L115–L118.
- Liu, X., Shemansky, D.E., 2006. Analysis of electron impact ionization properties of methane. *J. Geophys. Res.* 111, A04303–A04319.
- Liu, X., Heays, A.N., Shemansky, D.E., Lewis, B.R., Feldman, P.D., 2009. Analysis of terrestrial thermospheric N<sub>2</sub> c<sub>4</sub><sup>1</sup>Σ<sub>g</sub><sup>+</sup>(0) ~ b<sup>1</sup>Σ<sub>u</sub><sup>+</sup>(1) – X<sup>1</sup>Σ<sub>g</sub><sup>+</sup> dayglow emission observed by the Far Ultraviolet Spectroscopic Explorer. *J. Geophys. Res.* 114, D07304–D07318.
- Lopez-Moreno, J.J. et al., 2008. Structure of Titan's low altitude ionized layer from the Relaxation Probe onboard Huygens. *Geophys. Res. Lett.* 35, L22104. doi:10.1029/2008GL035338.
- Meier, R.R., Samson, J.A., Chung, Y., Lee, E.-M., He, Z.-X., 1991. Production of N<sup>+</sup> from N<sub>2</sub> + hν: Effective EUV emission yields from laboratory and dayglow data. *Planet. Space Sci.* 39, 1197–1207.
- Molina-Cuberos, G.J., Lopez-Moreno, J.J., Rodrigo, R., Lara, L.M., O'Brien, K., 1999. Ionization by cosmic rays of the atmosphere of Titan. *Planet. Space Sci.* 47, 1347–1354.
- Molina-Cuberos, G.J., Lopez-Moreno, J.J., Rodrigo, R., 1999. Chemistry of the galactic cosmic ray induced ionosphere of Titan. *J. Geophys. Res.* 104, 21997–22024.
- Molina-Cuberos, G.J., Lammer, H., Stumptner, W., Schwingenschuh, K., Rucker, H.O., Lopez-Moreno, J.J., Rodrigo, R., Tokano, T., 2001. Ionospheric layer induced by meteoric ionization in Titan's atmosphere. *Planet. Space Sci.* 49, 143–153.
- Molina-Cuberos, G.J., Schwingenschuh, K., Lopez-Moreno, J.J., Rodrigo, R., Lara, L.M., Anicich, V., 2002. Nitriles produced by ion chemistry in the lower ionosphere of Titan. *J. Geophys. Res.* 107, 5099. doi:10.1029/2000JE001480.
- Mount, G.H., Warden, E.S., Moos, H.W., 1977. Photoabsorption cross sections of methane from 1400 to 1850 Å. *Astrophys. J.* 214, L47–L49.
- Müller-Wodarg, I.C.F., Yelle, R.V., Cui, J., Waite Jr., J.H., 2008. Horizontal structures and dynamics of Titan's thermosphere. *J. Geophys. Res.* 113, E10005. doi:10.1029/2007JE003033.
- Nicolas, C., Alcaraz, C., Thissen, R., Vervloet, M., Dutuit, O., 2003. Dissociative photoionization of N<sub>2</sub> in the 24–32 eV photon energy range. *J. Phys. B* 36, 2239–2251.
- Niemann, H.B. et al., 2005. The abundances of constituents in Titan's atmosphere from the GCMS instrument on the Huygens probe. *Nature* 438. doi:10.1038/nature04122.
- Porco, C.C. et al., 2005. Imaging of Titan from the Cassini spacecraft. *Nature* 434, 159–168.
- Rees, H.M., 1989. *Physics and Chemistry of the Upper Atmosphere*. Cambridge University Press.
- Samson, J.A.R., Masuoka, T., Pareek, P.N., Angel, G.C., 1987. Total and dissociative photoionization cross sections of N<sub>2</sub> from threshold to 107 eV. *J. Chem. Phys.* 86, 6128–6132.
- Samson, J.A.R., Haddad, G.N., Masuoka, T., Pareek, P.N., Kilcoyne, D.A.L., 1989. Ionization yields, total absorption, and dissociative photoionization cross sections of CH<sub>4</sub> from 110–950 Å. *J. Chem. Phys.* 90, 6925–6932.
- Samson, J.A., Chung, Y., Lee, E.-M., 1991. Excited ionic and neutral fragments produced by dissociation of N<sub>2</sub><sup>+</sup> H band. *J. Chem. Phys.* 95, 717–719.
- Shemansky, D.E., Liu, X., 2005. Evaluation of electron impact excitation of N<sub>2</sub> X<sup>1</sup>Σ<sub>g</sub><sup>+</sup>(0) into the N<sub>2</sub><sup>+</sup> X<sup>2</sup>Σ<sub>g</sub><sup>+</sup>(v), A<sup>2</sup>Π<sub>u</sub><sup>+</sup>(v), and B<sup>2</sup>Σ<sub>u</sub><sup>+</sup>(v) states. *J. Geophys. Res.* 110, A07307. doi:10.1029/2005JA011062.
- Sittler, E.C., Hartle, R.E., Bertucci, C., Coates, A., Cravens, T., Dandouras, I., Shemansky, D., 2009. Energy deposition processes in Titan's upper atmosphere and its induced magnetosphere. In: Brown, R.H., Lebreton, J.-P., Waite, J.H. (Eds.), *Titan from Cassini–Huygens*. Springer.
- Sittler, E.C. et al., 2010. Saturn's magnetospheric interaction with Titan as defined by Cassini encounters T9 and T18: New results. *Planet. Space Sci.* 58, 327–350.
- Stamnes, K., Rees, M.H., 1983. Heating of thermal ionospheric electrons by suprathermal electrons. *Geophys. Res. Lett.* 10, 309–312.
- Stevens, M.H., 2001. The EUV airglow of Titan: Production and loss of N<sub>2</sub> c<sub>4</sub>(0)-X. *J. Geophys. Res.* 106, 3685–3689.
- Strobel, D.F., Shemansky, D.E., 1982. EUV emission from Titan's upper atmosphere: Voyager 1 encounter. *J. Geophys. Res.* 87, 1361–1368.
- Strobel, D.F., Meier, R.R., Strickland, D.J., 1991. Nitrogen airglow sources: Comparison of Triton, Titan, and Earth. *Geophys. Res. Lett.* 18, 689–692.
- Strobel, D.F., Atreya, S.K., Bezdard, B., Ferri, F., Flasar, F.M., Fulchignoni, M., Lellouch, E., Müller-Wodarg, I., 2009. Atmospheric structure and composition, in Titan from Cassini–Huygens. In: Brown, R.H., Lebreton, J.-P., Waite, J.H., Jr. (Eds.), *Springer*, pp. 235–257.
- Tabata, T., Shirai, T., Sataka, M., Kubo, H., 2006. Analytic cross sections for electron impact collisions with nitrogen molecules. *Atomic Data Nucl. Data Tabl.* 92, 375–406.
- Tomasko, M.G., Doose, L., Engel, S., Dafoe, L.E., West, R., Lemmon, M., Karkoschka, E., See, C., 2008. A model of Titan's aerosols based on measurements made inside the atmosphere. *Planet. Space Sci.* 56, 669–707.
- Vuitton, V., Yelle, R.V., McEwan, M.J., 2007. Ion chemistry and N-containing molecules in Titan's upper atmosphere. *Icarus* 191, 722–742.
- Vuitton, V., Yelle, R.V., Cui, J., 2008. Formation and distribution of benzene on Titan. *J. Geophys. Res.* 113. doi:10.1029/2007JE002997.
- Vuitton, V., Lavvas, P., Yelle, R.V., Galand, M., Wellbrock, A., Lewis, G.R., Coates, A.J., Wahlund, J.-E., 2009. Negative ion chemistry in Titan's upper atmosphere. *Planet. Space Sci.* 57, 1558–1572.
- Wang, J.-H., Liu, K., Min, Z., Su, H., Bersohn, R., Preses, J., Larese, J.Z., 2000. Vacuum ultraviolet photochemistry of CH<sub>4</sub> and isotopomers. II. Product channel fields and absorption spectra. *J. Chem. Phys.* 113, 4146–4152.

- Walter, C.W., Cosby, P.C., Helm, H., 1993.  $N(^4S^0)$ ,  $N(^2D^0)$ , and  $N(^2P^0)$  yields in predissociation of excited singlet states of  $N_2$ . *J. Chem. Phys.* 99, 3553–3561.
- Wilson, E.H., Atreya, S.K., 2004. Current state of modeling the photochemistry of Titan's mutually dependent atmosphere and ionosphere. *J. Geophys. Res.* 109, E06002. doi:10.1029/2003JE002181.
- Yelle, R.V., Vuitton, V., Lavvas, P., Klippenstein, S.J., Smith, M.A., Horst, S.M., Cui, J., 2010. Formation of  $NH_3$  and  $CH_2NH$  in Titan's upper atmosphere. *Faraday Discuss.* 147, 1–18. doi:10.1039/c004787m.
- Zipf, E.C., Espy, P.J., Boyle, C.F., 1980. The excitation and collisional deactivation of metastable  $N(^2P)$  atoms in auroras. *J. Geophys. Res.* 85, 687–694.